What Sets the Star Formation Rate of Molecular Clouds? The Density Distribution as a Fingerprint of Compression and Expansion Rates

N.B. When citing this work, cite the original published paper.

(article starts on next page)

What Sets the Star Formation Rate of Molecular Clouds? The Density Distribution as a Fingerprint of Compression and Expansion Rates

Sabrina M. Appel[1] , Blakesley Burkhart[1,2] , Vadim A. Semenov[3] , Christoph Federrath[4,5] , Anna L. Rosen[6,7,8] , and Jonathan C. Tan[9,10]

[1] Department of Physics and Astronomy, Rutgers University, 136 Frelinghuysen Rd., Piscataway, NJ 08854, USA; appel@physics.rutgers.edu
[2] Center for Computational Astrophysics, Flatiron Institute, 162 Fifth Avenue, New York, NY 10010, USA
[3] Center for Astrophysics | Harvard & Smithsonian, 60 Garden St., Cambridge, MA 02138, USA
[4] Research School of Astronomy and Astrophysics, The Australian National University, Canberra, ACT 2611, Australia
[5] Australian Research Council Centre of Excellence in All Sky Astrophysics (ASTRO3D), Canberra, ACT 2611, Australia
[6] Department of Astronomy, San Diego State University, San Diego, CA 92182, USA
[7] Computational Science Research Center, San Diego State University, San Diego, CA 92182, USA
[8] Department of Astronomy & Astrophysics, University of California, San Diego, La Jolla, CA 92093, USA
[9] Department of Space Earth & Environment, Chalmers University of Technology, Gothenburg, SE-412 96, Sweden
[10] Department of Astronomy, University of Virginia, Charlottesville, VA 22904, USA
Received 2023 January 2; revised 2023 June 14; accepted 2023 July 17; published 2023 August 25

Abstract

We use a suite of 3D simulations of star-forming molecular clouds, with and without stellar feedback, magnetic fields, and driven turbulence, to study the compression and expansion rates of the gas as functions of density. We show that, around the mean density, supersonic turbulence promotes rough equilibrium between the amounts of compressing and expanding gas, consistent with continuous gas cycling between high- and low-density states. We find that the inclusion of protostellar jets produces rapidly expanding and compressing low-density gas. We find that the gas mass flux peaks at the transition between the lognormal and power-law forms of the density probability distribution function (PDF). This is consistent with the transition density tracking the post-shock density, which promotes an enhancement of mass at this density (i.e., shock compression and filament formation). At high densities, the gas dynamics are dominated by self-gravity: the compression rate in all of our runs matches the rate of the run with only gravity, suggesting that processes other than self-gravity have little effect at these densities. The net gas mass flux becomes constant at a density below the sink formation threshold, where it equals the star formation rate. The density at which the net gas mass flux equals the star formation rate is one order of magnitude lower than our sink threshold density, corresponds to the formation of the second power-law tail in the density PDF, and sets the overall star formation rates of these simulations.

Unified Astronomy Thesaurus concepts: Interstellar medium (847); Star formation (1569); Star forming regions (1565); Giant molecular clouds (653); Protostars (1302); Theoretical models (2107)

1. Introduction

Stars form from the gravitational collapse of cold, dense gas within giant molecular clouds (GMCs), which are super-sonically turbulent, magnetized, and self-gravitating (e.g., Padoan et al. 1997; McKee & Ostriker 2007; Kennicutt & Evans 2012; Myers et al. 2014; Krumholz et al. 2018). Models of star formation must include how self-gravity and magneto-hydrodynamical processes interact with stellar feedback (i.e., the injection of momentum and energy from young stars) and the galactic environment to produce gas that collapses into stars (Collins et al. 2012; Padoan et al. 2012; Burkhart et al. 2017). To this end, the volume density probability distribution function (PDF) is a commonly used tool for analytic models of star formation that provides insight into the distribution of gas within GMCs (e.g., Krumholz & McKee 2005; Hennebelle & Chabrier 2008, 2009, 2011; Padoan & Nordlund 2011a, 2011b; Federrath & Klessen 2012; Hopkins et al. 2012; Padoan et al. 2014; Burkhart 2018). Models based on the density PDF have been useful in understanding a wide variety of physical processes, and are also commonly used in subgrid models to

model star formation in galaxy simulations (e.g., Braun & Schmidt 2015; Semenov et al. 2016, 2021; Trebitsch et al. 2017; Rosdahl et al. 2018; Kretschmer & Teyssier 2020; Gensior et al. 2020).

The shape of the density PDF for gas within GMCs (for both volume densities and column densities) has been well studied (see, e.g., Vazquez-Semadeni 1994; Vazquez-Semadeni et al. 1997; Passot & Vázquez-Semadeni 2003; Klessen 2000; Vaz-quez-Semadeni & Garcia 2001; Federrath et al. 2008; Kritsuk et al. 2011b; Burkhart & Lazarian 2012; Collins et al. 2012; Federrath & Klessen 2013; Imara & Burkhart 2016; Chen et al. 2019; Appel et al. 2022; Ma et al. 2022). It is well understood that supersonic turbulence produces a lognormal distribution in the density PDF and that self-gravity produces a power-law tail in dense, star-forming gas (see, e.g., Kainulainen et al. 2009; Ballesteros-Paredes et al. 2011; Alves et al. 2017; Burkhart 2018; Burkhart & Mocz 2019; Jaupart & Chabrier 2020). At the highest densities, the density and column density PDFs show evidence of an additional power-law tail (Schneider et al. 2015; Khullar et al. 2021). Schneider et al. (2015) observe a second power-law tail at the high-density end of the column density PDFs of star-forming regions and suggest several possible explanations for this second power-law tail, including the presence of an accretion disk or entrained gas due to protostellar feedback. Simulations further suggest that the first power-law forms due to collapse under the

influence of self-gravity while the second forms at higher densities due the formation of accretion disks around protostars (Khullar et al. 2021).

Previous work has also shown how the shape of the density PDF changes with the inclusion of different physical processes including supersonic turbulence, self-gravity, magnetic fields, and stellar feedback, as well as how the PDF changes in time as gas is exchanged between low- and high-density regions and eventually converted to stars (e.g., Burkhart 2018; Burkhart & Mocz 2019; Appel et al. 2022). In particular, Appel et al. (2022) showed that the inclusion of protostellar outflows can produce an excess of diffuse gas in the volume density PDF. This work also showed how diffuse, turbulently supported gas (the lognormal portion of the density PDF) is transferred into dense, gravitationally collapsing gas (the power-law portion of the density PDF), which in turn collapses into stars at the highest densities. Wang et al. (2010) similarly find that the dense gas depleted by forming stars is constantly replenished.

The density PDF alone provides limited information regarding the gas dynamics. Appel et al. (2022) provided an analysis of the time evolution of the density PDFs of simulated star-forming regions to determine how gas flows between different density regimes, which traced the dynamical evolution of the gas. In particular, Appel et al. (2022) showed that the high-density power-law tail of the density PDF is stable in time, suggesting that the diffuse gas rapidly replenishes the power-law tail as the dense gas is converted into or accreted by protostars. This suggests a connection between the density PDF and the gas dynamics that we explore further in this paper.

In this work, we explore the gas dynamics in a suite of 3D magnetohydrodynamic (MHD) simulations of star-forming regions. We connect the density PDF of simulated star-forming regions to the compression and expansion rates of the gas and compare these rates to the star formation rates (SFRs) of the simulated regions. In particular, we quantify the gas dynamics using the divergence of the gas velocities ($\nabla \cdot \boldsymbol{v}$, where $\boldsymbol{v}$ is the gas velocity), which traces the expanding (positive divergence) and gravitationally collapsing gas (negative divergence), respectively. Hence, the velocity divergence can be used as a metric to understand the compression and expansion rates of the gas, and can be used to quantify how the gas dynamics affect the SFR of star-forming molecular clouds. As we will show in this work, the compression and expansion rates can be converted to a net gas mass flux from low to high densities, which can be directly compared to the SFR of our simulations. By examining both the compression and expansion rates and the gas mass flux as functions of density, we are able to compare these quantities to the shape of the density PDF to determine how various physical processes, such as magnetic fields, turbulence, and stellar feedback, impact the gas dynamics.

This paper is organized as follows. Section 2 describes the simulations that are used in our analysis. Section 3 reviews the theory of the density PDF and how it connects to the SFR, and introduces our model for calculating the compression and expansion rates that we use in our analysis. Section 4 describes our simulation results and our analysis of the gas dynamics in our simulations. Finally, we discuss our results in Section 5, and our key conclusions are summarized in Section 6.

2. Simulations and Numerical Parameters

We use a suite of five simulations that were run with the FLASH MHD code (Fryxell et al. 2000), where each

simulation increases in complexity by including additional physical processes—gravity, turbulence driving, magnetic fields (i.e., MHD), and stellar feedback—so that we can separate how each of these processes affects the SFR, the gas density distribution, and the gas dynamics. The first four simulations in this suite are identical in their basic parameters to the study in Federrath (2015), which compared the SFR between runs with (1) gravity only, (2) as simulation (1), but also including turbulence, (3) as simulation (2), but also including magnetic fields, and (4) as simulation (3), but also including protostellar outflow (jet) feedback. Here, we redo these runs (with different turbulence seeds and at higher resolution), and we add a fifth simulation, which is set up the same as simulation (4), but also includes protostellar heating feedback. In Appendix C, we also consider a sixth simulation that is identical to simulation (5) but with decaying turbulence instead of continuously driven turbulence. Details of the runs are provided below.

2.1. Simulation Code and Initial Conditions

The general setup for all of our runs follows that of Federrath (2015), which uses the equation of state and hydrodynamics, gravity, and sink particles methods described in Federrath et al. (2014). The new aspects of the fifth run (run GTMJR) are the protostellar heating setup, as described in Federrath et al. (2017b) and updated in Mathew & Federrath (2020). We summarize key aspects of the setup of our runs here.

FLASH is a publicly available hydrodynamics code that uses adaptive mesh refinement (AMR; Berger & Colella 1989) and can include many interoperable modules (Fryxell et al. 2000; Dubey et al. 2008). The MHD solver used to run the simulations presented here uses a Godunov-type method using a second-order, five-wave approximate Riemann solver, termed HLL5R (Waagan et al. 2011). The self-gravity of the gas is modeled with a multigrid Poisson solver (Ricker 2008). We solve the 3D, ideal MHD equations with gravity (as described in Federrath et al. 2014):

$$\frac{\partial \rho}{\partial t} + \nabla \cdot (\rho \boldsymbol{v}) = 0, \tag{1}$$

$$\rho \left(\frac{\partial}{\partial t} + \boldsymbol{v} \cdot \nabla \right) \boldsymbol{v} = \frac{(\boldsymbol{B} \cdot \nabla) \boldsymbol{B}}{4\pi} - \nabla P_{\mathrm{tot}} + \rho \boldsymbol{g}, \tag{2}$$

$$\frac{\partial \boldsymbol{B}}{\partial t} = \nabla \times (\boldsymbol{v} \times \boldsymbol{B}), \tag{3}$$

$$\nabla \cdot \boldsymbol{B} = 0, \tag{4}$$

where ρ is the usual gas volume density, $\boldsymbol{v}$ is the gas velocity, $P_{\mathrm{tot}} = P_{\mathrm{th}} + 1/(8\pi)|\boldsymbol{B}|^2$ is the thermal and magnetic pressure, and $\boldsymbol{B}$ is the magnetic field. The gravitational acceleration of the gas, $\boldsymbol{g}$, is determined by both the self-gravity of the gas and the gravitational influence of the sink particles (Federrath et al. 2014):

$$\boldsymbol{g} = -\nabla \Phi_{\mathrm{gas}} + \boldsymbol{g}_{\mathrm{sinks}}; \tag{5}$$

$$\nabla^2 \Phi_{\mathrm{gas}} = 4\pi G \rho. \tag{6}$$

Our simulations are also set up with a polytropic equation of state to account for the thermal evolution of the gas. The equation of state is described by Federrath et al. (2014):

$$P_{\mathrm{th}} = K \rho^{\Gamma}, \tag{7}$$

Table 1
Overview of Key Simulation Parameters

Parameter	Value
Mean density (ρ_0)	3.28×10^{-21} g cm^{-3}
Initial total mass (M_{tot})	388 $M_\odot$
Box size (L)	2 pc
Velocity dispersion (σ_v)	1 km s^{-1}
Sonic Mach number ($\mathcal{M}_s$)	5
Driving parameter (ζ)	0.5
Virial parameter (α_{vir})	1.0
Magnetic field (B)	10 μG
Alfvénic Mach number ($\mathcal{M}_A$)	2.0
Max. effective resolution (N_{res}^3)	1024^3

Note. Note that quantities such as the mean density, total mass, and magnetic field strength refer to the initial values for each run, and the turbulence parameters (velocity dispersion, sonic Mach number, and driving parameter) refer to the values that result from the turbulence driving method.

with a polytropic exponent of

$$
\Gamma = \begin{cases}
1 & \text{for} & \rho \leqslant \rho_1 \equiv 2.50 \times 10^{-16}\text{g cm}^{-3} \\
1.1 & \text{for} & \rho_1 \leqslant \rho \leqslant \rho_2 \equiv 3.84 \times 10^{-13}\text{g cm}^{-3} \\
1.4 & \text{for} & \rho_2 \leqslant \rho \leqslant \rho_3 \equiv 3.84 \times 10^{-8}\text{g cm}^{-3} \\
1.1 & \text{for} & \rho_3 \leqslant \rho \leqslant \rho_4 \equiv 3.84 \times 10^{-3}\text{g cm}^{-3} \\
5/3 & \text{for} & \rho < \rho_4.
\end{cases}
\tag{8}
$$

This equation of state is discussed in greater detail in Federrath et al. (2014) and is modeled after the simulations by Masunaga & Inutsuka (2000). We note, however, that for the runs presented here, the sink formation threshold (discussed further below in Section 2.3) corresponds to a volume density of $\rho_{\text{sink}} = 2.07 \times 10^{-17}$ g cm^{-3}, which is lower than the first density threshold for the polytropic exponent. This means that gas will form sinks before reaching densities at which the equation of state would no longer be isothermal. Our runs are thus effectively isothermal, with the exception of the proto-stellar heating module described in Section 2.5.

Table 1 summarizes the key parameters of our simulation suite. Each simulation has a computational box size of 2 pc and periodic boundary conditions. The initial total gas mass for each simulation is 388 $M_\odot$, and each run is initialized with a uniform density of $\rho_0 = 3.28 \times 10^{-21}$ g cm^{-3}. This corresponds to a virial parameter of $\alpha_{\text{vir}} = 1.0$ after turbulence driving has established a fully developed turbulent cloud with a velocity dispersion of 1 km s^{-1} (details on the driving method are provided below).

2.2. Grid Refinement

Two levels of AMR are used. The base grid (level (1)) has a uniform resolution of 512^3 grid cells to capture the turbulence well (Kitsionas et al. 2009; Federrath et al. 2010; Price & Federrath 2010; Kritsuk et al. 2011a). At the highest level of AMR (level (2)), the cell size is 402.9 au, corresponding to a maximum effective grid resolution of $N_{\text{res}}^3 = 1024^3$ cells. Refinement is based on the Jeans length, requiring that the simulations resolve the Jeans length by at least 30 grid cells at any time and any point in space (Federrath et al. 2011). This is a much higher refinement of the Jeans length than required to

simply avoid artificial fragmentation (Truelove et al. 1997), which only requires 4 cells per Jeans length. The reason to prefer a Jeans resolution of at least 30 grid cells is that it allows us to capture solenoidal motions and minimum magnetic field amplification via the turbulent dynamo process (Federrath 2016a) on the Jeans scale (Federrath et al. 2011).

2.3. Star Formation

To model the formation of stars in each simulation, we use the sink particle method described in Federrath et al. (2010). When gas collapses under the influence of gravity and the density in a given cell reaches the sink formation density threshold, a sink particle is formed (if the gas also meets several additional criteria, as discussed below). Sink particles represent a star-disk system and only form on the highest AMR level. While the sink particles represent unresolved star-disk systems, we are unable to discern how much mass is in each component and, therefore, when we calculate the SFR (in Section 4), we assume the sink mass is representative of the star.

The sink formation density is (Federrath et al. 2010, 2014)

$$
\rho_{\text{sink}} = \frac{\pi c_s^2}{G \lambda_J^2} = \frac{\pi c_s^2}{4\,G r_{\text{sink}}^2},
\tag{9}
$$

where c_s is the sound speed, G is the gravitational constant, λ_J is the local Jeans length, and r_{sink} is the sink radius. The sink particle radius is set to 2.5 grid cell lengths (Federrath et al. 2010, 2014) to avoid artificial fragmentation (Truelove et al. 1997). Before a sink particle is formed from the gas above the density threshold given by Equation (9), the gas surrounding the cell that exceeds this density undergoes a series of checks for collapse. Only if the gas is bound and collapsing within a Jeans length centered on the cell that exceeds ρ_{sink} is a sink particle created. This procedure avoids artificial creation of sink particles in unbound regions where the density can exceed ρ_{sink} merely due to shock compression rather than gravitational collapse (see quantifications and discussions in Federrath et al. 2010).

Existing sink particles can accrete gas if that gas is within r_{sink} of the sink particle, above ρ_{sink}, and bound and collapsing toward the sink particle. The gravitational interactions between gas and sink particles and between the sink particles themselves is computed by direct summation using spline gravitational softening within r_{sink}. Please see Federrath et al. (2010, 2014) for details on the sink particle method.

2.4. Turbulence Driving

To drive turbulence, we use the methods described in Federrath et al. (2010), with the code publicly available on GitHub (Federrath et al. 2022). In summary, this uses an Ornstein–Uhlenbeck (OU) process to evolve the Fourier modes of the turbulent acceleration field used to drive the turbulence in real space. We generate Fourier modes in an interval between wavenumbers $k/(2\pi/L) = 1$ and 3, with amplitudes following a parabola, such that the peak of the parabola is at $k/(2\pi/L) = 2$, and the driving amplitude is exactly zero at $k/(2\pi/L) = 1$ and 3. Based on this, the driving scale is at $k/(2\pi/L) = 2$ in Fourier space, i.e., at $\ell_{\text{turb}} = L/2 = 1$ pc in real space. The amplitude is adjusted such that the resulting velocity dispersion is $v_{\text{turb}} = 1$ km s^{-1} (which corresponds to a sonic Mach number of $\mathcal{M} = 5$; considering the sound speed

Table 2
Summary of Simulations

	Simulation	Turbulence?	B-fields?	Jets?	Heating Feedback?	SFR ($M_\odot$ yr^{-1})	$N_{\rm sinks}$	ρ_* (g cm^{-3})
1	G	No	No	No	No	12.7×10^{-5}	75	N/A
2	GT	Yes	No	No	No	5.60×10^{-5}	20	8.03×10^{-19}
3	GTM	Yes	Yes	No	No	2.58×10^{-5}	4	5.38×10^{-19}
4	GTMJ	Yes	Yes	Yes	No	1.50×10^{-5}	18	1.20×10^{-18}
5	GTMJR	Yes	Yes	Yes	Yes	1.40×10^{-5}	22	1.79×10^{-18}

Notes. All simulations include self-gravity. Turbulence indicates whether turbulence continues to be driven throughout the simulation run. When turbulence driving is turned off, the velocity field is also set to zero, as discussed below. B-fields indicates whether magnetic fields are included. Jets refers to the inclusion of protostellar outflows, and heating feedback refers to the inclusion of radiative feedback in the form of radiative heating (Mathew & Federrath 2020). SFR refers to the average star formation rate for each simulation between SFE = 2%, and SFE = 10% (the SFE range used in Figures 6 through 8) and is the value plotted in Figures 7 and 8. $N_{\rm sinks}$ indicates the final number of sinks each simulation formed by SFE = 10%. The $\rho_* = \rho_0\, e^{s_*}$ values are the densities at which the net gas mass flux matches the SFR, as discussed in Section 4.5, and are shown as black stars in Figure 8.

$c_{\rm s} = 0.2\,{\rm km\,s^{-1}}$ for molecular gas at about 10 K) in the fully developed turbulent state.

This defines a turbulent turnover time, as the combination of the driving scale and the target velocity dispersion, namely $t_{\rm turb} = \ell_{\rm turb}/v_{\rm turb} \sim 1$ Myr. The autocorrelation timescale of the OU process is set to this timescale, producing a turbulent acceleration field that varies smoothly in space and time. The turbulence is fully developed (resulting in a fully developed turbulent cloud) after about $2\,t_{\rm turb}$ (Federrath et al. 2010; Price & Federrath 2010), at which point we activate gravity and allow for star formation based on the criteria defined in the previous subsection. This procedure is identical to previous works (e.g., Federrath & Klessen 2012; Federrath 2015; Mathew & Federrath 2021; Nam et al. 2021).

Here, we use a natural mixture of solenoidal and compressive modes in the turbulence driving (acceleration) field (Federrath et al. 2008). This is controlled by performing a Helmholtz decomposition of the acceleration field in Fourier space, and mixing the modes together, as desired (see details in Federrath et al. 2010, which defines the turbulence driving mode mixture parameter ζ. A purely solenoidal driving field is obtained with $\zeta = 1$, and a purely compressive driving field is obtained with $\zeta = 0$. The natural mixture of driving modes corresponds to $\zeta = 0.5$, not to be confused with the ratio of the density dispersion to sonic Mach number, referred to as $b = \sigma_\rho/(\rho_0\,\mathcal{M})$ and where $b \sim 0.38$ in the case of naturally mixed driving (see Figure 8 in Federrath et al. 2010), which is an indirect consequence of the driving on the density and velocity fields, while ζ is the parameter that directly controls the mode mixture in the turbulence driving (acceleration) field.

All simulations discussed here use exactly the same turbulence driving sequence and random seed to drive the turbulence. However, we note that, when magnetic fields are included, the density structure at the start of the star formation stage of the simulations is not identical to the density field without magnetic fields, as the fields naturally alter the density and velocity structure of the clouds. Apart from that, however, runs (1) (G) and (2) (GT; both without magnetic fields), and runs (3) (GTM), (4) (GTMJ), and (5) (GTMJR; all with magnetic fields), respectively, have exactly identical density and velocity fields at the beginning of the star formation stage (with the exception of run (1) (G), where the velocity field is completely removed at the start of the star formation stage). Each of these runs and the differences in their setups are discussed below and summarized in Table 2.

2.5. Model Variations

Figure 1 shows density projection plots for all 5 of our simulations, and Table 2 summarizes the parameters that change between each simulation, as well as selected key results, such as the average SFR.

The first simulation (run G) only includes self-gravity. To set up this simulation run, turbulence is driven as described above for two turbulent turnover times to fully establish the turbulence, at which point turbulence driving is stopped, all gas velocities are set to 0, and the cloud is set to be in pressure equilibrium (to have constant pressure throughout the simulation domain while keeping $\gamma = 1.1$). Finally, self-gravity is turned on. This setup ensures an identical initial density distribution between run G and the subsequent run GT (which includes turbulent velocities and driving), before allowing the gas to collapse under the influence of only gravity, without any contribution from either turbulent driving or decaying turbulence.

The second simulation (run GT) is initialized identically to run G. However, unlike run G, we do not alter the gas velocities or gas pressure after the initial driving period, and the turbulent driving continues with the same turbulent driving parameter and sonic Mach number once the gravity is turned on.

The third simulation (run GTM) is initialized identically to run GT, except for the addition of a magnetic field. Following the setup described in Federrath (2015) and Mathew & Federrath (2021), the initial magnetic field is assumed to be uniform along the $\hat{z}$ direction where $B_z = 10\,\mu$G. The turbulent driving during the initial two turnover times mixes the magnetic field orientation such that the field is no longer uniform by the time gravity is turned on, and an additional turbulent magnetic field component is established (Federrath 2016a). The total magnetic field, together with the turbulent velocity field, corresponds to an Alfvén Mach number of 2 in the fully developed turbulent regime. Our chosen magnetic field strength is based on the typical values observed in Falgarone et al. (1992) and Crutcher et al. (2010). In particular, Falgarone et al. (2008) measure an Alfvén Mach number of ∼1.5 at scales similar to our simulations.

The final two simulations are identical to run GTM, but also include stellar feedback. In runs GTMJ and GTMJR, the sink particles produce two-component protostellar outflows that consist of a fast collimated jet and a slower, wide-angle outflow similar to observed disk winds. This two-component model approximates the overall features of observed jets and is described in detail in Federrath et al. (2014). Run GTMJR
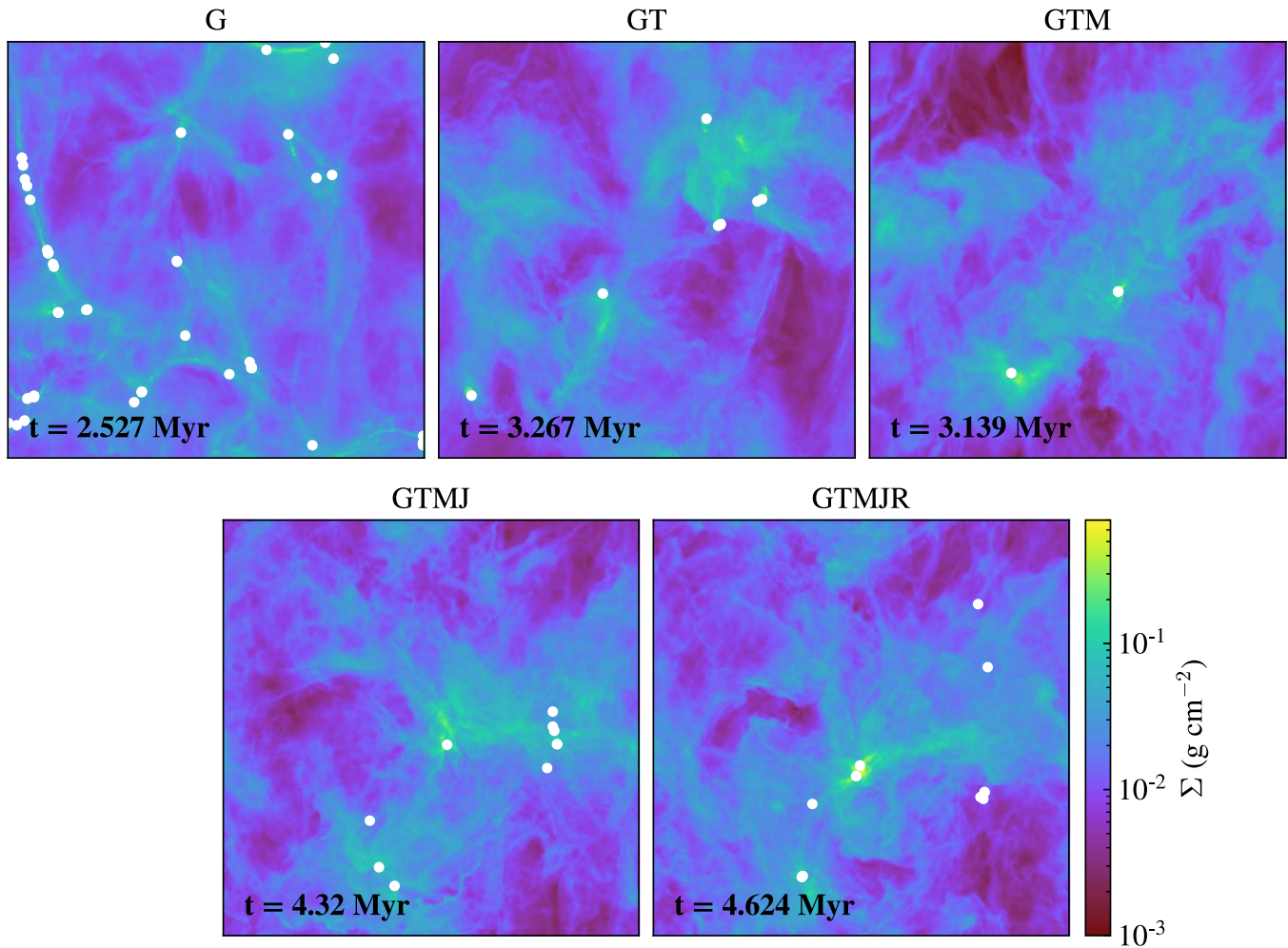
Figure 1. Density projection plots for each of the simulations described in Table 2 at snapshots where the SFE is approximately 5%. The corresponding times since gravity is turned on are shown on the plot ($t_0 = 0$ is defined as the point at which gravity is turned on for each simulation). The projected positions of sink particles are shown as white circles.

additionally includes radiative heating from the sink particles, as first introduced in Federrath et al. (2017a), and updated in Mathew & Federrath (2020). The polar heating model described in Mathew & Federrath (2020) sets up the radiation to be predominantly bipolar rather than isotropic since the sink particle represents a star-disk system and the disk will shield equatorial radiation (Rosen et al. 2016). This radiative feedback model only includes heating (and neglects photoionization and radiation pressure). However, for low-mass star formation, radiative heating is the dominant effect of radiative feedback, and this model compares reasonably well with low-mass star formation simulations that include radiative transfer (Offner et al. 2009). As we will show, the highest-mass sink particle that forms in run GTMJR (the only run that implements this radiative feedback model) is $5.6\,M_\odot$. Therefore, we conclude that only including radiative heating is a reasonably accurate description of radiative feedback for this run (Mathew & Federrath 2020).

The simulations presented in this work that include turbulence (runs GT, GTM, GTMJ, and GTMJR) drive turbulence continuously as the simulation evolves. To determine if turbulence driving may have an effect on our results, we also include a simulation identical to run GTMJR except that we turn off turbulence driving once gravity is turned on (i.e., at $t = 0$). In this run (run GTMJRD), the turbulence cascade is then

allowed to decay self-consistently as the simulation progresses. We compare this additional simulation to run GTMJR in Appendix C. As expected (see, e.g., Federrath 2015; Appel et al. 2022), the average SFR for this run is higher than that in run GTMJR and increases over the course of the run as the turbulence decays. However, in general, our key results regarding the compression and expansion rates and the gas mass flux are not significantly changed.

3. Analysis Methods

Appel et al. (2022) investigated both the shape of the density PDF and how different parts of the density distribution evolve in time, beginning to give insight into the dynamics of the gas. In this work, we continue to investigate the gas dynamics by considering the gas compression and expansion rates as a function of density. In this section, we first introduce the density PDF, and then we introduce the calculation of the compression and expansion rates, which we will use to study the gas dynamics that can be related to the SFR.

3.1. The Density PDF

Many analytic models of star formation assume a time-independent, lognormal density PDF, as suggested by the statistics of supersonic turbulence (e.g., Krumholz & McKee 2005;

Hennebelle & Chabrier 2011; Padoan & Nordlund 2011a; Federrath & Klessen 2012). However, recent work suggests a piecewise lognormal plus power-law density PDF is a better fit for gas that includes both turbulence and gravity (e.g., Imara & Burkhart 2016; Chen et al. 2019; Khullar et al. 2021; Ma et al. 2022). The piecewise density PDF as proposed by Burkhart (2018) takes the form

$$p_{\mathrm{LN+PL}}(s) = \begin{cases} N \dfrac{1}{\sqrt{2\pi}\,\sigma_s} e^{-\frac{(s-s_0)^2}{2\sigma_s^2}} & s < s_{\mathrm{t}} \\ N C e^{-\alpha s} & s > s_{\mathrm{t}}, \end{cases} \qquad (10)$$

where σ_s and s_0 are the width and the mean of the lognormal portion, respectively, and α is the slope of the power-law portion.

As discussed in Section 1, the density PDF is a key component of many analytic star formation models, including subgrid models for the SFR. In these models, the density PDF is used to quantify the gas mass fraction that can form stars (because it is dense enough to collapse), and, weighted by a freefall time factor, predict the SFR. The density PDF therefore quantifies how much of the gas is primarily turbulent versus how much gas is collapsing.

The SFR can be calculated by integrating over the density PDF above a critical density for star formation and multiplying by the appropriate timescales and densities (see, e.g., Krumholz & McKee 2005; Hennebelle & Chabrier 2011; Padoan & Nordlund 2011a; Federrath & Klessen 2012; Burkhart 2018). The critical density (s_{crit}) can be defined in a number of ways; Federrath & Klessen (2012) give a thorough overview of several commonly used critical densities (see also Burkhart 2018, and references therein). Ultimately, each definition of the critical density finds a way to characterize the density at which gravity becomes dynamically important. For example, Krumholz & McKee (2005) directly compares the scales at which gravity and turbulence become equal, i.e., the sonic scale (Federrath et al. 2021). Alternatively, Burkhart (2018) suggests that the critical densities discussed in Federrath & Klessen (2012) are effectively traced by the transition density (s_{t}) where the lognormal density PDF changes to a power-law PDF. The transition between these regimes serves as evidence within the density PDF of the fact that gravity becomes dynamically dominant (Burkhart 2018; Burkhart & Mocz 2019).

In our analysis, we explore how different physical processes impact the gas dynamics and how these dynamics are reflected in the density PDF. Thus, we are particularly interested in investigating the density at which self-gravity dominates over other physical processes and how the gas density PDF relates to the SFR. Hence, we will investigate if the transition density, s_{t}, from Burkhart (2018) is the density at which gravity becomes dynamically dominant and sets the stage for star formation.

3.2. Calculating the Compression Rate

The density PDF describes the density distribution of the gas at a single point in time, but it can be connected to the underlying gas dynamics with the continuity equation. We quantify the rate of change of the density using the Lagrangian formulation of the continuity equation, which is given by

$$\frac{D\rho}{Dt} + \rho(\nabla \cdot \boldsymbol{v}) = 0 \,, \qquad (11)$$

where we use $D/Dt \equiv \partial/\partial t + \boldsymbol{v} \cdot \nabla$ as a shorthand for the Lagrangian derivative (see Appendix A for derivation).

To compare this expression to the density PDF, which we have calculated in terms of the natural logarithm of the normalized density,

$$s = \ln(\rho/\rho_0) \,, \qquad (12)$$

we rearrange Equation (11) to be expressed in terms of s (see Appendix A for details):

$$\frac{Ds}{Dt} \equiv -(\nabla \cdot \boldsymbol{v}). \qquad (13)$$

Thus, we have a connection between the time evolution of the natural logarithm of the normalized density (the Ds/Dt term) and the gas dynamics (as represented by the velocity vector, $\boldsymbol{v}$).

Because s is dimensionless, the quantity Ds/Dt has dimensions of inverse time, i.e., it is the rate of change of the logarithmic density contrast s. This quantity represents the flow rate of gas into or out of a particular region of the simulation. *For the purpose of this study, we refer to positive values of Ds/Dt as compression rates and negative values of Ds/Dt as expansion rates.* Regions with a positive rate ($Ds/Dt > 0$) have net compressing gas, i.e., converging flows ($\nabla \cdot \boldsymbol{v} < 0$), which means that more gas is entering that region than is leaving it. Conversely, regions with a negative rate ($Ds/Dt < 0$) have net expanding gas, i.e., diverging flows ($\nabla \cdot \boldsymbol{v} > 0$), which means that more gas is leaving that region than is entering it.

We compute the compression rate, Ds/Dt, for every simulation cell using the yt package (Turk et al. 2011). We calculate the gradient of each component of the velocity field, which we then use to construct the divergence of the velocity field

$$\frac{Ds}{Dt} = -(\nabla \cdot \boldsymbol{v}) = -(\partial_x v_x + \partial_y v_y + \partial_z v_z). \qquad (14)$$

Thus, for every cell in the simulation, we now have both a density value and a compression or expansion rate, and we can investigate how the compression and expansion rates behave as functions of time and how they compare to the density PDF.

4. Results

4.1. Star Formation throughout Each Run

We first compare the impact of the different physical processes in each simulation by examining the integrated star formation efficiency (SFE) and the SFR for each simulation. In the upper panel of Figure 2, we show the SFE as a function of time for each of the simulations, where the integrated SFE is defined as

$$\mathrm{SFE} = \frac{M_*}{M_{\mathrm{init}}}, \qquad (15)$$

where M_* is the total stellar mass formed, and M_{init} is the initial cloud mass. Figure 2 demonstrates that the SFE evolves at very different rates for each simulation due to the different physical properties that are included in each run. To account for this difference when the various runs are compared, we use SFE to characterize the evolutionary stage of the simulation in addition to the simulation time. For example, Figure 1 shows density projections of snapshots at SFE $\approx 5\%$.
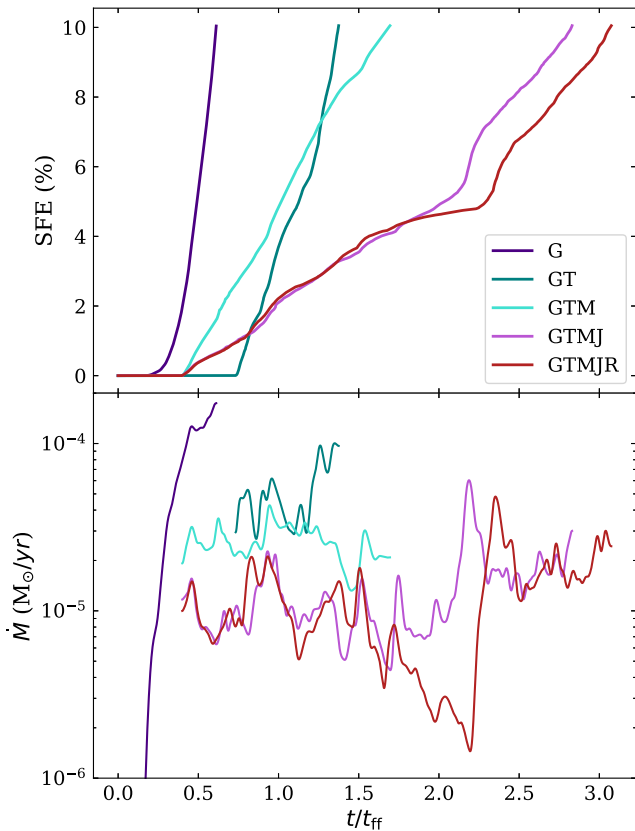
Figure 2. The integrated star formation efficiency (SFE; top panel) and the star formation rate (SFR; bottom panel) as a function of time for each of the simulations described in Table 2. The $t_0 = 0$ point is defined to be the point at which gravity is turned on for each simulation. As additional physical processes are included, the SFR drops, and it takes longer for each simulation to reach a similar integrated SFE.

The evolution of the SFR—which directly relates to the slope of the SFE as a function of time—is plotted in the lower panel of Figure 2. Although there is a lot of variation over time in the SFR for all of the simulations, there is a clear overall decrease in the SFR as more physical processes are included. This is also evident in the mean SFR values shown in Table 2. This decrease in the SFR with the inclusion of additional physics has been seen and quantified in previous studies (see, e.g., Wang et al. 2010; Federrath 2015).

As an additional diagnostic of the variations between each simulation, we consider the masses of the individual sink particles as a function of time. In Figure 3, we plot the mass growth of each individual sink particle as a function of time, and Table 2 reports the final number of sink particles (N_{sinks}) for each run. We see that run G (the far-left panel) forms a large number of sink particles, but only forms relatively low-mass ($< 4\ M_\odot$) sink particles throughout the simulation. Run GT forms fewer, higher-mass sink particles compared to run G. The inclusion of magnetic fields results in yet less fragmentation due to additional magnetic support, and run GTM forms only four sink particles, including two that reach up to $\sim 14\ M_\odot$. The inclusion of jet feedback, however, increases fragmentation (Wang et al. 2010; Federrath et al. 2014; Guszejnov et al. 2020; Mathew & Federrath 2021), and runs GTMJ and GTMJR both produce a greater number of sink particles that are all 5.8 $M_\odot$ or less.

From both Figures 2 and 3, we can see that there is very little difference between runs GTMJ and GTMJR. The inclusion of

radiative feedback in run GTMJR slightly slows down star formation relative to run GTMJ, which only includes proto-stellar jet feedback. Similarly, the inclusion of radiative feedback does not substantially change the amount of fragmentation, as seen in Figure 3 and Table 2. Thus, we choose to omit run GTMJ in our subsequent analysis, because it is very similar to run GTMJR. We include some further discussion of this run in Appendix B.

4.2. Expansion and Compression Rates as Functions of Density

In Figure 4, we compare the density PDF to the compression and expansion rates for a single snapshot of run GT where the SFE $\cong 0.5\%$. Given the value of Ds/Dt for every cell in the simulation, we can split up all of the gas in the simulation into expanding and compressing gas and consider the density PDF for each component of the gas. We plot the compression and expansion rates in separate panels because the collapsing and expanding gas trace different density regimes. In particular, the collapsing gas traces higher densities and includes higher rate values than those of the expanding gas. Thus, the top panels of Figure 4 show the separate volume-weighted density PDFs for the expanding gas (solid line; left panel) and the compressing gas (solid line; right panel). For comparison, the overall density PDF (dotted lines) is also shown. In the bottom panels of Figure 4, we show the compression and expansion rates, Ds/Dt, given by Equation (14) in units of Myr^{-1} versus $s = \ln(\rho/\rho_0)$ as a 2D histogram (the heat maps in the bottom two panels of Figure 4). The left panel shows the 2D histogram of the expansion rate as a function of s of the expanding gas (gas with a negative Ds/Dt), and the right panel shows the corresponding histogram for the compression rate of the compressing gas (gas with a positive Ds/Dt). We also show the median compression and expansion rates as a function of density with the interquartile range shown as a shaded region. For comparison, we show the freefall rate (i.e., the reciprocal of the gravitational freefall time) as a function of density, as given by

$$\frac{1}{t_{\mathrm{ff}}} = \left(\frac{3\pi}{32\, G\, \rho} \right)^{-1/2}. \tag{16}$$

From this plot, we can see that the expanding gas contributes more to the overall PDF at low densities as compared to the compressing gas. Conversely, at high densities, the overall density PDF is primarily composed of compressing gas. Indeed, at densities $s \gtrsim 5$, the compressing gas PDF and the overall PDF are essentially identical, and the expansion rate dramatically drops off, meaning that compression dominates in this portion of the PDF. As we will see in the subsequent analysis, this density is the point at which the gas mass flux equals the SFR in our simulations. This is also the density range where we see the development of a second power-law tail in the PDF, in agreement with previous work (see, e.g., Khullar et al. 2021).

In Figure 4, we show the density PDFs for only a single snapshot of a single simulation. However, the same trend (e.g., the overall PDF matching the expanding gas PDF at low densities and the compressing gas PDF at high densities) is apparent for all physics cases and throughout the run of the simulations. Appendix D shows examples of the density PDF for several physics cases and multiple points in time.

A comparison of top and bottom panels shows that some aspects of the distribution of the heat map correspond to the
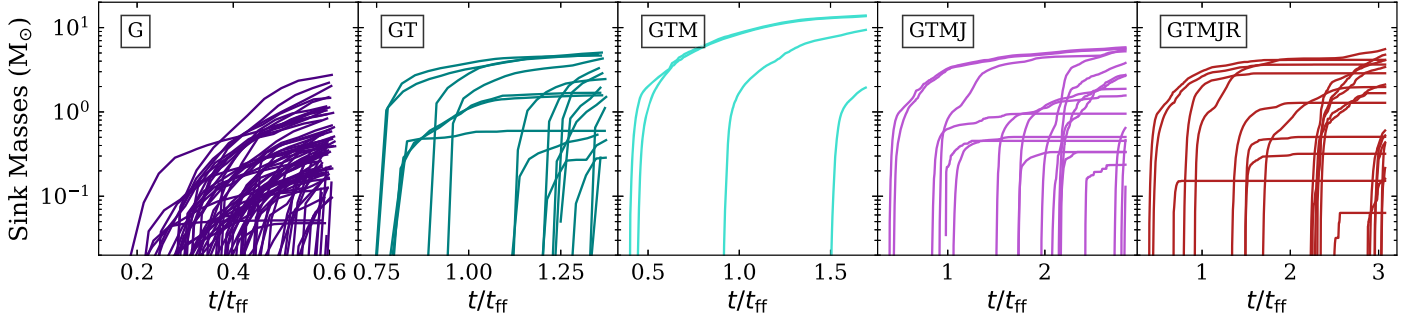
Figure 3. The evolution of the masses of individual sink particles as a function of time for each of the simulations described in Table 2. Each sink particle follows a single line on the plot. The $t_0 = 0$ point is defined to be the point at which gravity is turned on for each simulation. Each run takes a different amount of time to form the first sink particle. Thus, note that the x-axis range varies for each panel.
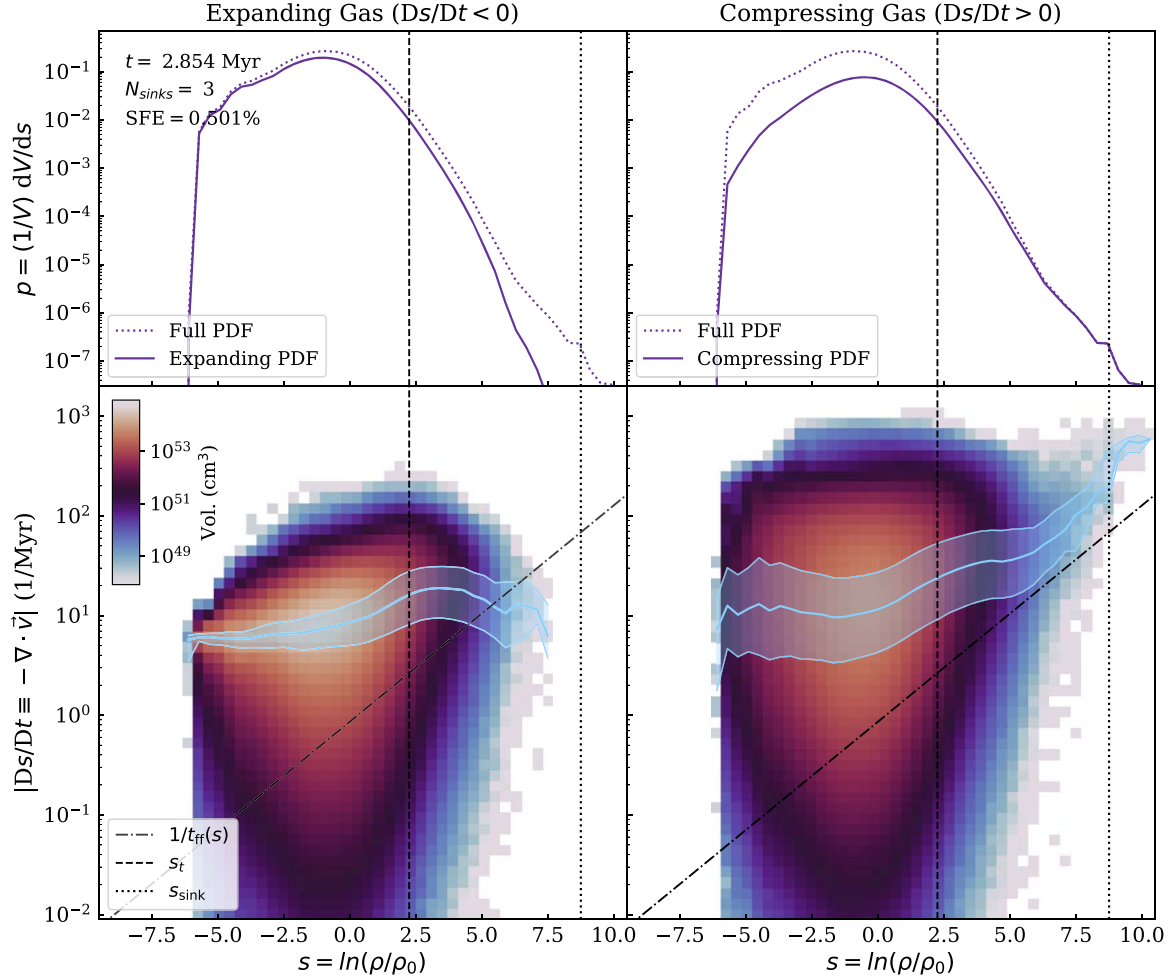

Figure 4. The density PDFs and histograms of the compression and expansion rates for a single snapshot of run GT where the SFE $\approx 0.5\%$. Top: the volume-weighted density PDF for all of the gas in the simulation region (dotted line) and the volume-weighted density PDF for only the expanding gas ($Ds/Dt < 0$; left column) or only the compressing gas ($Ds/Dt > 0$; right column) within the simulation region. Bottom: a 2D, volume-weighted histogram of the expansion rate as a function of density for only the expanding gas ($Ds/Dt < 0$; left column) or of the compression rate as a function of density for only the compressing gas ($Ds/Dt > 0$; right column). The corresponding median rate as a function of density (with the 25th to 75th percentiles) is shown as a blue line (and shaded region). The freefall rate as a function of density is overplotted. All: for all panels, the transition density (s_t) from Appel et al. (2022) is overplotted as a vertical dashed line. The sink formation density threshold (s_{sink}) for the simulation is also shown as a dotted vertical line. Key information (time, number of sink particles, and integrated SFE) for the particular snapshot shown here is indicated on the plot.

shape of the density PDF. In particular, there are many fewer counts and less spread in the compressing gas at high densities where the density PDF has a lower value. Indeed, there is very little gas at all at high densities in the expanding gas heat map.

Meanwhile, there is a higher concentration of gas at average to low densities in the expanding gas heat map than in the compressing gas heat map. The heat maps emphasize that for both expanding and compressing gas there is a lot of spread in

the rate values, with gas at a wide variety of rates at most densities. However, the median line and the interquartile range indicate that the majority of the gas is clustered around a particular rate for a given density. For example, the median expansion rate drops at high densities, while the median compression rate increases at high densities.

4.3. The Effect of Different Physics on Gas Compression and Expansion Rates

Figure 5 shows the rate–density plots for our four main simulations (runs G, GT, GTM, and GTMJR). All four physics cases are shown at an approximate midpoint of each simulation, corresponding to SFE $\cong 5\%$ (the corresponding times are shown on the plot). Again, we show the expanding gas for a given snapshot in the left-hand panels and the compressing gas in the right-hand panels.

Progressing from the top of the figure to the bottom, we can see how the rate–density plot changes as different physical processes are added. The top row of Figure 5 shows run G, which only includes self-gravity. The rate–density plot for this case shows a few distinctive features. First, the median line of the compressing gas follows or is slightly above the freefall rate at all densities. In contrast, the expanding gas has a relatively flat distribution around the mean density and only increases toward the freefall rate at higher densities. At densities above $s \gtrsim 4$, the compressing gas collapses at a rate faster than freefall, likely a consequence of the details of the density distribution and the gas dynamics at these densities. We discuss this behavior, and possible explanations, further in Sections 4.4 and 5.

However, in the second row of Figure 5, we see that the median rate for run GT has an elevated and approximately flat distribution for both the expanding and compressing gas at all densities below the transition density (vertical dashed line), suggesting that turbulence reduces the density dependence of the compression and expansion rates below s_t. Above s_t, the compressing gas initially rises slower than the freefall rate. At densities above $s \gtrsim 5$, the compression rate begins to rise parallel to the freefall rate, and at densities above $s \gtrsim 7$, the compression rate rises faster than the freefall rate. Meanwhile, the expanding gas remains flat at densities above s_t, before turning slightly down at densities above $s \gtrsim 7$. This suggests that, for gas below $s \sim 5$, the turbulence increases both the rate of convergence and the rate of divergence of the gas relative to the freefall rate. Above $s \sim 5$, the behavior of the compressing gas is similar to the behavior of run G, suggesting that the dynamics of the compressing gas at these densities is mostly determined by gravity.

In the third row of Figure 5, we see that the inclusion of magnetic fields has a less prominent effect than the difference between run G and run GT. However, it still produces some differences in the rate–density plot. In particular, the median rate of the compressing gas near the mean density becomes lower than that in run GT. This suggests that magnetic fields serve to dampen the effects of turbulence on compressing gas. Furthermore, in regions where magnetic pressure dominates over self-gravity, the time it takes for gas to collapse increases since magnetic pressure provides support against gravitational collapse. Hence, the collapse of gas in these regions to higher densities is delayed. At high densities, the compressing gas grows faster than the freefall rate, similar to the behavior of run

G at these densities. This behavior suggests that magnetic pressure is subdominant to self-gravity above s_t.

In the final row of Figure 5, we see that the inclusion of protostellar outflows has an impact on the lowest-density gas. This is in agreement with the findings of Appel et al. (2022), which show that protostellar outflows produce an excess of low-density gas. The plots that include protostellar outflows show the same evidence of the rate flattening at densities near the mean density as in run GTM. The compressing gas rate for this run also grows at faster than the freefall rate at the highest densities, as in the other runs. However, run GTMJR also shows a large upturn in the rate of the very lowest-density gas—for both compressing and expanding gas. This suggests that protostellar outflows are producing both rapidly expanding and rapidly compressing low-density gas. The compressing low-density material is likely associated to the bow shocks produced by the jets as they propagate through and entrain low-density gas.

4.4. Net Compression and Expansion Rates

In Figure 6, we show the median compression and expansion rates as in Figure 5, but now averaged over time. We take the median in time for snapshots between SFE $= 2\%$, and SFE $= 10\%$ in order to avoid fluctuations in the compression and expansion rates that we see at early times. These fluctuations at early times likely reflect the fact that it takes a while for the simulations to settle into an approximate steady state, and we exclude this transient period from our analysis. All four simulations are shown with the 1σ variations shown as shaded regions around the median values. The leftmost panel shows the median rate for the expanding gas, and the central panel shows the median rate for the compressing gas. The rightmost panel of Figure 6 shows the net rate, which we calculate by taking the volume-weighted average of all of the expanding gas rates and the compressing gas rates for a single density bin for a single snapshot. We then plot the median in time of this net rate in the rightmost panel of Figure 6.

Similar to the median lines for individual snapshots seen in Figure 5, we see that distributions of the median rates in Figure 6 vary with the inclusion of additional physical processes. The gravity-only simulation (run G) has a very low and flat distribution of expanding gas for densities around the mean density, in accordance with the lack of any turbulent velocities. The net rate for run G increases with density, close to the freefall rate for all densities, especially at low densities.

The other simulations, which all include turbulent velocities and driving, have generally flatter (i.e., almost independent of density) distributions of rates around the mean density. Importantly, the turbulence-driven rates of gas expansion and compression at these densities ($s < 5$; see Figures 5 and 6) have comparable magnitudes and are much higher than the freefall rate at the same densities (dashed-dotted line). This statistical equilibrium between compression and expansion is indicative of continuous gas cycling between the self-gravitating, high-density gas in the power-law tail, out of which stars form, and the low-density, non-star-forming gas that corresponds to the lognormal portion of the density PDF (Appel et al. 2022; see also Semenov et al. 2017, 2018 for analogous processes in the galactic context).

At high densities, we see that the rate of the compressing gas for all simulations increases with density faster than the freefall rate at densities well above s_t (e.g., $s \gtrsim 5$). The fact that all of
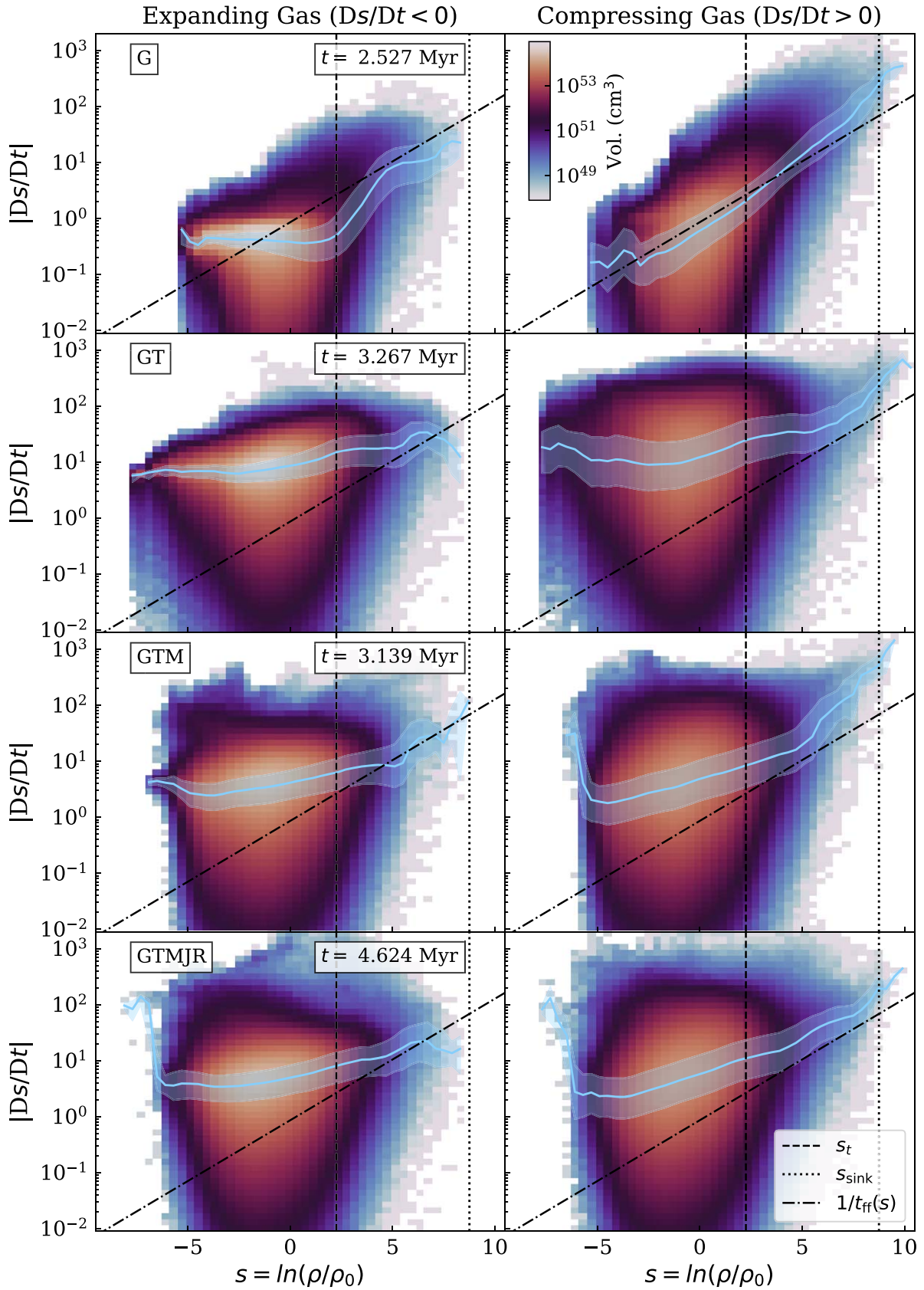
Figure 5. Each row is the same as the bottom panels of Figure 4 and shows the 2D, volume-weighted histograms of the expansion and compression rates as a function of density. Each row shows a single snapshot of a different simulation. The snapshots chosen for this plot all have SFE ≈ 5%, and the time since gravity was turned on is shown on the plot for each snapshot.

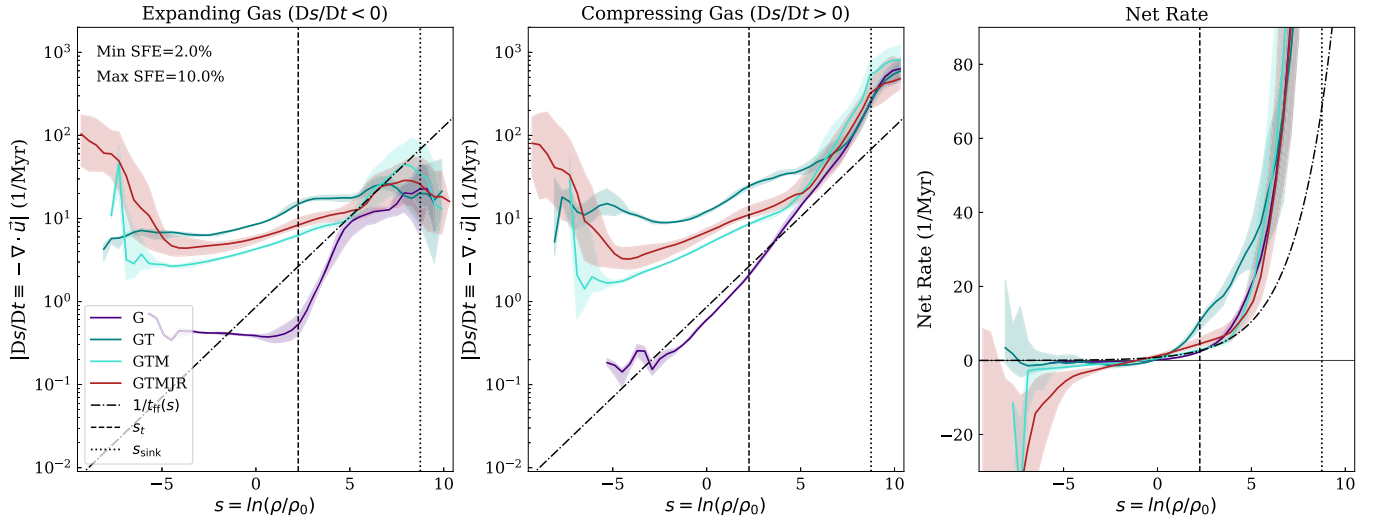**Figure 6.** The median in time ($\pm 1\sigma$ variation in time) of the median rates for the expanding gas ($Ds/Dt < 0$; left panel) and for the compressing gas ($Ds/Dt > 0$; center panel). The rightmost panel shows the median in time ($\pm 1\sigma$ variation in time) of the net rate on a linear scale. The freefall rate as a function of density is overplotted in each panel, as is the transition density from Appel et al. (2022; vertical dashed line). The sink formation density (s_{sink}) for each of the simulations is also shown as a dotted vertical line.

the simulations converge on the same behavior as run G suggests that the compressing gas at high densities is strongly influenced by gravity in all cases. The faster-than-freefall collapse is likely a consequence of the details of the density distribution and the gas dynamics that is accreting onto the sink particles. In particular, the faster-than-freefall collapse may be a consequence of plotting the rate as a function of the s value of individual cells; since s is a cell-by-cell quantity, it may not reflect how the gas is actually distributed around the sinks and the resulting gravitational potential. Alternatively, this may indicate the influence of accretion processes. In particular, previous work suggests that $s \sim 5$ (which is where the net rate increases above freefall) is where the accretion disk forms around the sinks (i.e., Schneider et al. 2015; Khullar et al. 2021). This is also the density where the second power law forms in the density PDF (Federrath & Klessen 2013; Schneider et al. 2015; Burkhart 2018; Khullar et al. 2021).

In the net rate panel, we also see that, for densities above the mean density, all of the physics cases are dominated by compressing gas. Only at densities below the mean does the net rate take on a negative value for some of the physics cases, corresponding to the gas being dominated by expansion. This effect is most evident in the net rate of the run with feedback (run GTMJR), which takes on large negative values for the lowest-density gas (e.g., $s \lesssim -5$) as a result of the inclusion of protostellar jet feedback. Similarly, at the lowest densities, we see that both the expanding and compressing gas rises significantly for run GTMJR. This agrees with our understanding that jets drive gas out of dense regions and into low-density, rapidly expanding gas (see also Appel et al. 2022).

4.5. The Gas Mass Flux

In the previous sections, we considered the compression and expansion rates, which have dimensions of inverse time. By converting to a mass-weighted distribution of the rates versus density, we can calculate a gas mass flux in units of solar masses per year that we can compare directly to the SFR.

Let H_m be the mass-weighted version of the heat maps in Figures 4 and 5, or equivalently, the amount of mass at a given

compression (or expansion) rate bin, $\Delta\mathcal{R}$, and density bin, Δs. Then, the net gas mass flux (in solar masses per year) for a given density bin is the product of H_m and the compression rate, summed over every rate:

$$F_{\Delta s} = \sum_{\Delta\mathcal{R}} H_m \Delta\mathcal{R}. \qquad (17)$$

This gives us a net gas mass flux as a function of density, or a metric of how much gas is expanding or compressing in solar masses per year as a function of density. As with the net rate in Section 4.4, a negative net gas mass flux corresponds to net expanding gas, and, conversely, a positive net gas mass flux corresponds to net compressing gas.

To get the gas mass flux for only the compressing gas, we sum over all of the gas with positive rates. Similarly, to get the gas mass flux for only the expanding gas, we sum over all of the gas with negative rates.

We show the median in time of the gas mass flux for the expanding gas (left panel) and the compressing gas (right panel) in Figure 7, where the shaded regions show the 1σ variations in time. The net gas mass flux is shown in Figure 8. For both Figures 7 and 8, we again have only considered snapshots between SFE = 2%, and SFE = 10%. We overplot the mean SFR (also for the snapshots between SFE = 2%, and SFE = 10%) for each simulation as a horizontal line in both figures.

4.5.1. The Compressing and Expanding Gas Mass Flux

The fluxes of both compressing and expanding gas show prominent peaks near the mean density, $s = 0$. This is because there is much greater gas mass near $s = 0$, where the mass-weighted density PDF peaks, and the fluxes quickly fall off at higher and lower densities where the density PDF also falls off. Compression clearly dominates near s_{t}, which corresponds to the post-shock density where mass piles up due to shocks (Federrath 2016b). At even higher densities, the expansion rate exponentially drops off. At $s \approx 6$, the compressing gas mass flux flattens out before rising again at yet higher densities. As Figure 8 shows, this is also near the density at which the net gas
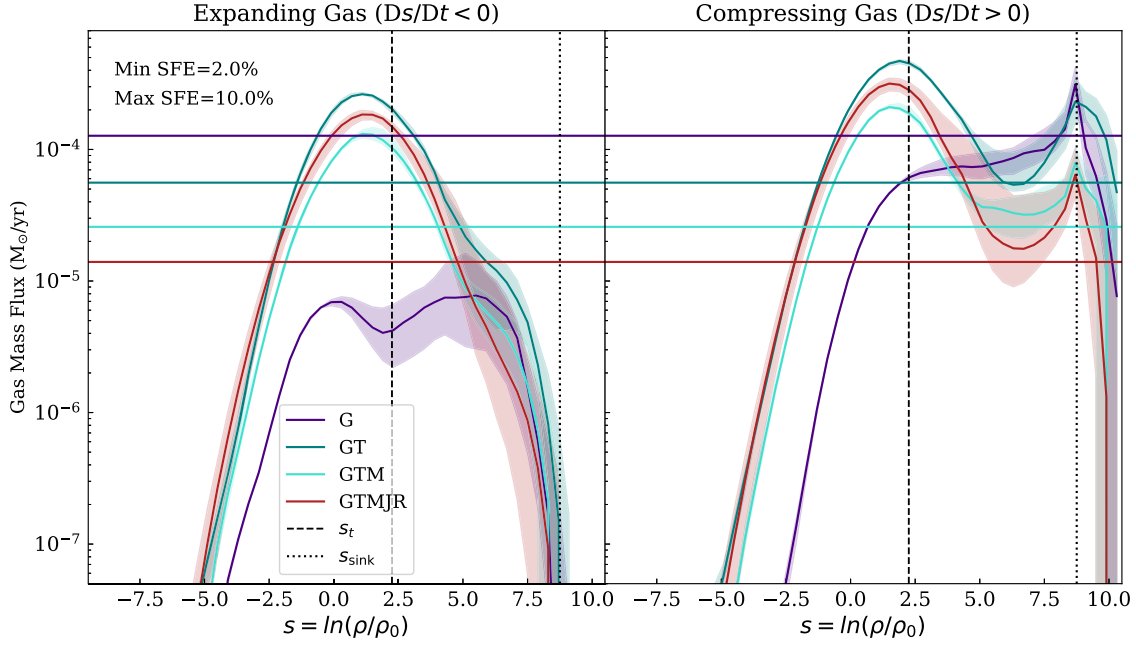
Figure 7. The median in time ($\pm 1\sigma$ variation in time) of the gas mass flux in units of solar masses per year for the expanding gas ($Ds/Dt < 0$; left panel) and for the compressing gas ($Ds/Dt > 0$; right panel). The average SFR of each run is overplotted as a horizontal line. As in Figure 6, the transition density from Appel et al. (2022) and the sink formation density (s_{sink}) for each of the simulations are also shown.
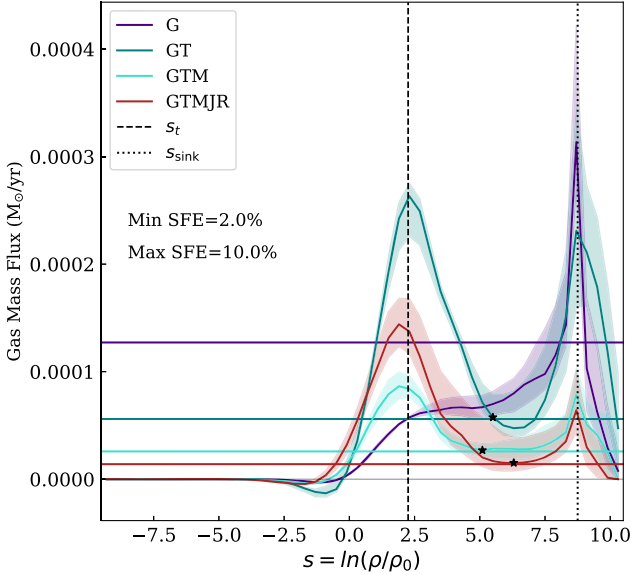

Figure 8. The median in time ($\pm 1\sigma$ variation in time) of the net gas mass flux. The average SFR of each run is overplotted as a horizontal line. The values of s_*, the densities at which the net gas mass flux meets the SFR, for each of the runs except run G are shown as black stars. The horizontal, thin, gray line shows the SFR = 0 line. As in Figure 6, the transition density from Appel et al. (2022) and the sink formation density (s_{sink}) for each of the simulations are also shown.

mass flux is roughly equal to the SFR (see a more detailed discussion below).

The compressing gas mass flux continues to increase above this density ($s \approx 6$) and peaks at s_{sink}. We investigated the formation of this second peak and found that it develops as sink particles start forming. In particular, right before the first sink particle is formed, no peak is present at s_{sink}, and the plateau in the compressing gas mass flux extends all the way to s_{sink}

(except for run G, which exhibits very different behavior, as discussed below). Therefore, this second peak is likely a numerical artifact resulting from the effects of limited resolution and of the sink particle model on the local gas dynamics.

Run G exhibits rather different behavior as a function of density and over time than the other runs. The median line shown in Figures 7 and 8 for run G has roughly constant compressing gas mass flux with increasing density above s_t up until $s \approx 6$, after which the compressing (and net) gas mass flux increases and peaks at S_{sink}. Unlike the other runs, however, before the peak at s_{sink} forms, there is not a plateau in the compressing gas mass flux at $s \approx 6$ for run G; instead, the compressing gas mass flux continues to decrease with increasing density above s_t until well after the first sink forms. Indeed, the peak in the compressing gas mass flux at s_{sink} for run G develops slowly over many snapshots after the first sink is formed, suggesting this increase in compressing gas mass flux is due to the presence of sink particles. Furthermore, the lack of plateau before the formation of the first sink particle confirms that this plateau in the compressing gas mass flux is a consequence of physical processes beyond gravity.

We also note that the density range at which the compressing gas mass flux begins to increase again for all of the runs ($s \approx 6$) corresponds to approximately the density at which the second power-law tail is expected to form in the density PDF, due to accretion disks beginning to form (see, e.g., Schneider et al. 2015; Khullar et al. 2021). Thus, the increase in flux just below the sink threshold density may also be influenced by the process of accretion onto sink particles.

The gas mass flux does fall off above s_{sink}, but as there is only a very small amount of gas at these densities and this is, by definition, above the density at which sinks form, it is unclear how much we can trust any metrics of the behavior of the gas at these densities.

4.5.2. The Net Gas Mass Flux

Looking at Figure 8, we see that the net gas mass flux is very close to zero at the lowest densities, corresponding to equal expanding and compressing gas mass flux, as expected for driven turbulence. At around the mean density, the net gas mass flux transitions rapidly to a positive value, indicating that gas at and above the mean density is net compressing. The transition to net compressing gas at approximately the mean density matches the behavior of the net rate in Figure 6, and is due to shock compression, which piles up gas from the mean density to overdensities, up to the isothermal jump-condition of M_s^2 (see, e.g., Padoan & Nordlund 2011b; Federrath 2016b, and references therein). The result of this shock compression is that the net gas mass flux peaks at the transition density, s_t, indicating a gas pileup and the formation of filamentary structures in the cloud.

Similar to the behavior of the compressing gas mass flux in Figure 7, the net gas mass flux decreases in all runs at densities greater than s_t, except run G (the purple line in Figure 8). As discussed, for run G, gravity is the only dynamical process controlling the the gas dynamics past s_t until sinks form. Therefore, the gas is moving with constant acceleration (hence the flat or increasing net gas mass flux between $s = s_t$, and $s \approx 5$). A given parcel of gas (with constant mass) should accelerate at a constant rate, and therefore, the net gas mass flux, which accounts for the amount of mass, should be approximately flat when gravity is the primary driver of the gas dynamics. For the other simulations, the addition of turbulence dramatically changes the gas dynamics at densities near to and higher than the post-shock density (i.e., the gas in the power-law portion of the density PDF). With driven supersonic turbulence, a strong peak at s_t in the gas mass flux confirms this density traces the post-shock density and the formation of filamentary features in the simulations (see, e.g., Padoan & Nordlund 2011b; Federrath 2016b). This is evident in Figure 8, which shows that the gas mass flux increases and reaches a maximum at the post-shock density where the gas is compressed. At $s > s_t$, gravity begins to significantly influence the gas dynamics. At this point, the density PDF forms the first power-law tail, and the gas mass flux decreases until it reaches either a local minimum or a plateau at around $s = 5$–6 (marked with a star symbol in Figure 8). At densities above this point (s_*), the other runs reflect the behavior of the gravity-only run, indicating that self-gravity plays a dominant role in setting the gas dynamics at the highest densities.

For ease of reference, we refer to the density at which the net gas mass flux first matches the mean SFR (after rising above the SFR at s_t) as s_*. The values of s_* for each of the runs except run G (which exhibits a very different behavior between s_t and s_{sink}, as discussed) are reported in Table 2 and are shown as black stars in Figure 8. The values in Table 2 and Figure 8 are calculated for the mean SFR and median gas mass flux between SFE = 2%, and SFE = 10%.

The falloff in the gas mass flux between s_t and s_* is due to the fact that the acceleration (i.e., derivative of the rate) is smaller than that suggested by freefall collapse, due to magnetic pressure and turbulent support, thereby slowing down collapse. The acceleration picks up at around $s = 5$–7, where an increase in the slope of the compression rate, shown in the middle panel of Figure 6, can be observed. At this point, the plateau develops, signaling a constant gas mass flux. Interestingly, the value of the gas mass flux at this plateau
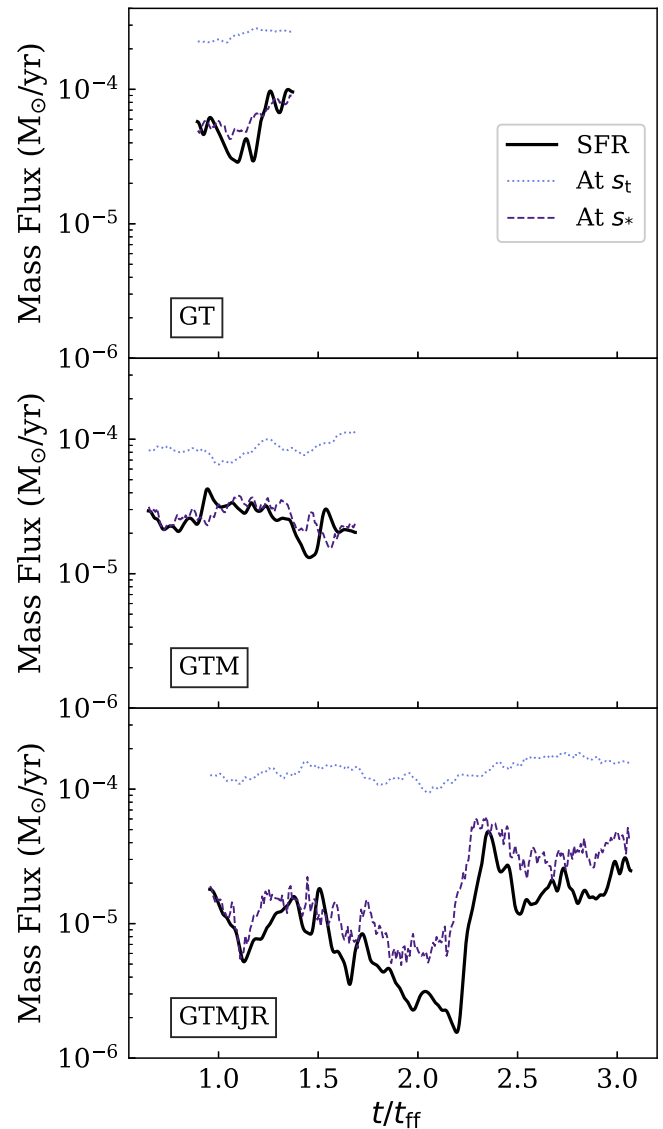

Figure 9. The net gas mass flux at two different fixed densities ($s = s_t$, and $s = s_*$) are plotted in comparison to the smoothed SFR as a function of time for each simulation. The net gas mass flux values are the time dependent counterparts to the values in Figure 8 and are measured at a single density bin with a center equal to or just above the corresponding density.

matches the mean SFR. At the highest densities, a strong peak develops around the sink threshold density, as mass is rapidly funneled into the sink particles.

4.5.3. Connecting the Gas Mass Flux and the SFR

We further investigate the relationship between s_*, the gas mass flux, and the SFR in Figure 9. First, we plot the smoothed SFR as a function of time for runs GT, GTM, and GTMJR. The SFR is smoothed using `scipy`'s `Gaussian_filter1d` function with a σ of $\sim$0.02 Myr. We also plot the net gas mass flux value at two key density bins: at s_t and at s_*. The values plotted in Figure 9 are the value of the net gas mass flux for each individual snapshot (sampled at every fifth snapshot to reduce noise) at the density bin that is at or just above the density of s_t or s_*. We note that we use the same value of s_* (the value in Table 2) for every snapshot, and, since this value is calculated based on where the median net gas mass flux meets the mean SFR, may not reflect exactly where the net gas

mass flux of an individual snapshot meets the SFR of that snapshot.

We find that, for all runs, the net gas mass flux at the transition density, s_t, is always higher than the SFR by at least a factor of 5, and by nearly 2 orders of magnitude at some points in time. This is consistent with Figure 8, which shows that the median gas mass flux near s_t is higher than the mean SFR for all three cases. This discrepancy likely corresponds to the core mass efficiency factor for star formation models, which take all the gas in the power-law tail portion of the density PDF as star-forming (Burkhart 2018). The core mass efficiency factor accounts for the fact that the inclusion of turbulence and magnetic fields makes the process of forming stars take much longer than freefall and that the inclusion of outflows cycles dense gas back to densities below s_t before it forms stars. This slow down of the formation of stars from dense, star-forming gas is clearly evident in the discrepancy between the net gas mass flux at s_t and the smoothed SFR. Furthermore, although the difference between the net gas mass flux at s_t and the SFR is largest (at most times) for run GTMJR, there is a significant discrepancy for all three runs shown in Figure 9, confirming that both turbulence and magnetic fields, and not only outflows, are contributing to preventing gas above the transition density from forming sink particles.

However, for all three runs, the net gas mass flux at s_* as a function of time closely matches the value of the SFR. Time variable features of the SFR are also found in the net gas mass flux at s_*. For example, there is a large jump in the SFR for run GTMJR around $t/t_{ff} \sim 2.2$ that is echoed by a similar jump in the net gas mass flux at s_*, but not in the gas mass flux at s_t. The similarity between the value of the net gas mass flux at s_* and the SFR indicates that the gas dynamics around s_* plays a key role in setting the SFR. We explore some of the implications of this connection in the Discussion section below.

5. Discussion

5.1. The Compression and Expansion Rates

Our work investigates the ways in which different physical processes affect the gas dynamics of star-forming regions as a function of density and how they are reflected in the density PDF shape. In density regimes where the influence of gravity is dynamically dominant (e.g., above the transition density s_t), the gas dynamics of the simulations that include turbulence does not completely match the behavior of the gravity-only run until densities above $s \gtrsim 5$ (i.e., at densities where self-gravity dominates). Only at the highest densities of compressing gas does the behavior of the compression rate become very similar for all of the simulations presented in this work. This suggests that turbulence, magnetic fields, and feedback act to significantly alter how much gas reaches the highest densities and influence the structure of collapsing regions.

Similarly, we see that turbulence acts to increase the rate of both the compressing and expanding gas at densities below the transition density. Below the transition density turbulence dominates, and the compressing and expanding motions balance out, resulting in a net rate that is near zero. Above the transition density, gravity dominates, and the net rate rises rapidly. We also find that the net gas mass flux peaks at s_t, suggesting that the density where the first power-law tail forms is an excellent tracer of the post-shock density (see, e.g., Padoan & Nordlund 2011b; Federrath 2016b).

In contrast to the effect of turbulence, magnetic fields act to decrease the rate of both the compressing gas and the expanding gas at most densities below the transition density, relative to the run with only turbulence and gravity. This suggests that magnetic pressure acts to dampen the increased motion from turbulence. We note that the difference in the median rate near the mean density is only about a factor of 2 (see Figure 6), and some contribution may be due to random variations. However, the fact that this difference is evident in the median in time quantities suggests that this change is unlikely to be due solely to random variations or the random seed. Further work is needed to understand how this decrease in the rate depends on the initial magnetic field strength and the initial random seed.

Finally, we see that the inclusion of protostellar outflows slightly increases the median rates of both the compressing gas and the expanding gas, relative to the run with magnetic fields (as seen in Figure 6), in agreement with the expectation that the inclusion of protostellar outflows will increase the kinetic energy of the gas (Appel et al. 2022). The most dramatic effect of protostellar outflows is on the lowest-density gas, where we see that protostellar outflows produce rapidly expanding and compressing low-density gas. In addition, the net rate (right-most panel in Figure 6) has a lot more variation in time for the cases with protostellar outflows at low densities, suggesting that the inclusion of protostellar outflows introduces significant time variation in the compression and expansion rates of the low-density gas carved out by outflows.

In Figure 6, we find that the compression rate increases with density faster than the freefall rate for all physics cases, once the density exceeds approximately $s \sim 5$. As discussed above in Section 4.4, this may be a consequence of plotting the rate as a function of s, when s is, by definition, a cell-by-cell measurement of the density, while the rate of collapse depends on the average density of the collapsing region. As the density of collapsing regions increases toward the center, the cells on the outskirts have lower densities, and therefore, their density changes at a faster rate than the freefall rate calculated locally for individual cells. This can explain the seemingly faster-than-freefall rate at high densities in Figure 6. In addition, calculations of the freefall rate typically assume a spherically symmetric density distribution, while the complex geometry of the flow can introduce deviations of the rate from the analytic freefall scaling.

This density also heralds the formation of the second power-law tail in these simulations, as studied by Schneider et al. (2015) and Khullar et al. (2021), and which roughly corresponds to the formation of accretion disks. This process of accretion onto the sinks may also contribute to the faster than freefall collapse seen in Figure 6, although our runs likely do not fully resolve accretion disks, making this connection uncertain. Regardless, the rate at which the gas passes through this density range appears to play a role in setting the SFR in our simulations (see Figures 8 and 9, and discussed below). Future work will determine how the accretion disk forms and how the gas mass flux and compression and expansion rates depend on the sonic Mach number, Alfvénic Mach number, and virial parameters.

In Section 4.2, we also explored the relationship between the compression and expansion rates and the density PDF. We see that the high-density end of the density PDF is most closely matched by the PDF of the compressing gas, and the low-

density end of the density PDF is most closely matched by the PDF of the expanding gas. This agrees with our understanding that the compressing gas is mostly at higher densities (that are dominated by gravity), and the expanding gas is mostly at lower densities where gravity is subdominant.

5.2. The Gas Mass Flux

The gas mass flux (Figure 7) combines information from the compression and expansion rates (Figure 6) and the overall density PDF. At low densities, the gas mass flux is low due to both low rates and small quantities of gas. Near the transition density from lognormal to power-law distributions, the gas mass flux peaks due to the formation of shocks (Federrath 2016b). The drop-off in the net gas mass flux above the transition density is evidence of various processes actively preventing collapse of the gas since the acceleration of the gas is stalled relative to freefall acceleration. The net gas mass flux declines until it reaches a constant value (i.e., it plateaus), analogous to a terminal velocity where the resistive forces are magnetic fields and turbulent motions. The net gas mass flux at this plateau matches the SFR at a density (s_*) that is well above the transition density. This behavior of the gas mass flux matches the fact that the analytical models of the SFR that integrate over all densities above the critical density require an additional efficiency factor, implying that not all of the gas above the critical density ends up in a star. This agrees with the fact that the gas mass flux at s_t is higher than the SFR before dropping off—there are processes preventing and delaying much of this gas from actually forming stars.

Schneider et al. (2015) observe the presence of a second power-law tail in the column density PDFs of star-forming regions. Similarly, Khullar et al. (2021) demonstrate the existence of a second power law in the density PDF that begins at densities greater than $s \sim 5$. The Khullar et al. (2021) model suggests that the lognormal portion of the density PDF is turbulence dominated, the first power law is gravity dominated, and the second power law (corresponding to the highest-density gas) is disk or rotation dominated. This suggests a possible interpretation for the behavior of the net gas mass flux at high densities. In particular, the point where the net gas mass flux matches the SFR (s_*) may correspond to the beginning of this second power law, and the increase in the net gas mass flux above s_* may be due to the influence of disk rotation. Although, again, our simulations do not fully resolve the disk accretion, meaning that further work is needed to verify this connection. As discussed above, however, the flux at which the gas passes through this density range appears to set the SFR in our simulations. This rate is highest in run GT and lower in the runs with feedback from protostellar outflows; hence, the SFR is lower when outflow feedback is included. This agrees with Khullar et al. (2019) who show that the star formation efficiency per freefall time increases dramatically at a high-density threshold that is different from the sink formation threshold. Further work is needed to confirm this connection and to compare the value of s_* found here to the s_d value from Khullar et al. (2021) and to the threshold from Khullar et al. (2019) above which the efficiency significantly increases.

5.3. Other Implications and Future Work

Our work may have important implications for subgrid models for isolated GMC simulations, or even galaxy

formation simulations. We demonstrated that the SFR is set by the gas mass flux at s_*. This can act as a minimum resolvable density required to set the SFR in simulations. However, measuring the gas mass flux peak and fitting a curve to higher densities could result in an empirical subgrid SFR model that could be used by simulations to resolve protostellar core physics. Doing so would require measuring $\nabla \cdot \boldsymbol{v}$ and determining where this is negative (i.e., where gas is compressing). Turning this into a gas mass flux (Figure 7) could then yield similar curves, which could be extrapolated to higher-than-resolved densities (i.e., protoplanetary disk densities) where the SFR is then set.

Future work will explore how this s_* density depends on the cloud mass, the virial parameter, the sonic Mach number, the Alfvénic Mach number, and the magnetic field properties. We would also like to study cases without driven turbulence and with and without self-consistent feedback driven turbulence. Future studies could also explore how the gas dynamics, and s_* in particular, changes with the inclusion of more realistic thermal physics, such as that associated with an ambient far-UV field and cosmic rays (e.g., similar to the thermal physics setup in Wu et al. 2017). As discussed, further work is also needed to understand the potential connection between the values of s_* and the s_d value from Khullar et al. (2021), as well as the role of disk rotation and accretion.

5.4. Limitations of the Current Setup and Future Work

Our current analysis focuses on a limited number of turbulent box simulations. Although this setup allows us to separately explore the effects of each physical process on the gas dynamics, our approach has certain limitations. We discuss some of these limitations here, as well as the ways that future work may address these limitations and build upon the present work.

In the current paper, we introduce our analysis of the gas dynamics using a limited number of simulations that explore the inclusion of varying physical processes, but do not fully explore the parameter space. The simulations analyzed here consider only a single value of the sonic Mach number, magnetic field strength, and virial parameter, as well as only a single type of turbulence driving. It will be critical for future work to analyze the impact of varying each of these parameters.

For example, previous work has shown that the magnetic field strength can have nonlinear effects on the structure of the gas and, thus, on the process of star formation (e.g., Passot et al. 1995; Ballesteros-Paredes & Mac Low 2002; Zamora-Avilés et al. 2018). Similarly, varying the sonic Mach number and virial parameter can dramatically affect the SFR, even suppressing star formation entirely (e.g., Federrath & Klessen 2012; Padoan et al. 2014). The current simulation suite is too limited to give insight into how the values of these parameters affect the compression and expansion rates or the net gas mass flux, and we leave the analysis of this parameter space to future work. Furthermore, we consider only a single magnetic field strength based on the typical magnetic field strengths observed for many regions of the interstellar medium (e.g., Falgarone et al. 2008; Hull et al. 2017). While this serves as an important comparison point with our runs without a magnetic field strength, it is worth considering how our results may change with different magnetic field strengths, which we leave for future work.

We also note that the simulations used in this paper utilize periodic boundary conditions. We envision our simulation regions to be representative of a high-density region that is embedded in a larger star-forming complex, i.e., that a similar process of star formation is happening on every side of our simulation region. As a result, the mean density of our simulations is higher than that observed for an entire molecular cloud, since it represents an overdense part of the cloud (e.g., Kainulainen et al. 2009; Stutz & Kainulainen 2015). However, this setup is unable to account for either in-falling gas from the surrounding medium or gas expulsion out of the star-forming region. Future work will need to be done to understand how the gas dynamics (and s_* in particular) change with different boundary conditions (e.g., such as those used in Lane et al. 2022; Lewis et al. 2023; Cournoyer-Cloutier et al. 2023). Furthermore, zoom-in simulations that model molecular clouds in the galactic context (e.g., such as the approach in Seifried et al. 2017) may provide an opportunity to investigate how the gas mass fluxes depend on the scale, i.e., from the scale of molecular clouds down to star-forming cores.

6. Conclusions

Previous work has presented evidence for the cycling of gas between different parts of gas density PDF within molecular regions: the high-density power-law tail, out of which stars form, and the non-star-forming lognormal portion at average and low densities (Appel et al. 2022). In this paper, we build on this analysis and further investigate the gas dynamics within star-forming regions using metrics such as the compression and expansion rates of the gas as a function of the gas density, and the gas mass flux through different portions of the density PDF.

We find the following:

1. The overall gas dynamics is dominated by compressing gas at densities above the mean density (corresponding to the power-law part of the density PDF), in agreement with the fact that the simulations are undergoing net gravitational collapse at high densities. In particular, at the highest densities, the net rate of all of our runs matches the net rate of the run with only gravity, suggesting that processes other than gravity have little effect at these densities.

2. At average to low densities (corresponding to the lognormal part of the density PDF), turbulence produces both compression and expansion, and results in a relatively constant rate, independent of gas density. This rate is significantly higher than the freefall rate at these low densities.

3. We find that the net gas mass flux peaks at the transition between the lognormal and power-law forms of the density PDF. This is consistent with the transition density tracking the post-shock density, which promotes an enhancement of mass at this density (i.e., shock compression and filament formation).

4. The inclusion of stellar feedback in the form of protostellar outflows has a significant effect on the gas dynamics at low densities where protostellar outflows result in very rapidly expanding and compressing gas.

5. For simulations that include turbulent velocities, the net gas mass flux above the transition density declines until it reaches a constant value (i.e., it plateaus). The net gas mass flux becomes constant at a density within the power-law tail, which we denote as s_*. The gas mass flux at s_* closely traces the SFR, despite it being a far lower density than the sink threshold. This suggests that the gas dynamics at this density, s_*, plays an important role in setting the SFR. We find that s_* varies slightly with the inclusion of different physics.

Appendix A
Eulerian and Lagrangian Continuity Equation

In Section 3.2, we use the Lagrangian formulation of the continuity equation. Here, we briefly show how to derive the Lagrangian formation of the continuity equation.

First, let us consider a fluid element of volume V and density ρ. The mass of this element remains constant in time, even as the density and volume may change. Thus,

$$\frac{D}{Dt}(\rho V) = 0 \iff V\frac{D\rho}{Dt} + \rho\frac{DV}{Dt} = 0, \quad (A1)$$

where we use D/Dt as a reminder that we are using the Lagrangian derivative. Considering only the second term of the

latter expression,

$$\frac{DV}{Dt} = \oint_A (\boldsymbol{v} \cdot \boldsymbol{A}) ds$$
$$= \int_V (\nabla \cdot \boldsymbol{v}) dV$$
$$= (\nabla \cdot \boldsymbol{v}) V, \tag{A2}$$

where $\boldsymbol{v}$ is the velocity field, $\boldsymbol{A}$ is the normal vector of the surface, and we have used the Divergence theorem to go from the first to the second line. We can then rewrite Equation (A1) as

$$V \frac{D\rho}{Dt} + \rho[(\nabla \cdot \boldsymbol{v})V] = 0$$
$$\frac{D\rho}{Dt} + \rho(\nabla \cdot \boldsymbol{v}) = 0, \tag{A3}$$

which gives us the familiar Lagrangian formulation of the continuity equation in terms of ρ, shown in Equation (11).

Since we wish to compare this expression to the density PDF, which we have calculated in terms of $s = \ln(\rho/\rho_0)$, we rearrange Equation (A3) in terms of s. First, we rewrite $\rho = \rho_0 e^s$. Then,

$$\frac{D}{Dt}(\rho_0 e^s) + (\rho_0 e^s)(\nabla \cdot \boldsymbol{v}) = 0;$$
$$(\rho_0 e^s) \frac{Ds}{Dt} + (\rho_0 e^s)(\nabla \cdot \boldsymbol{v}) = 0;$$
$$\frac{Ds}{Dt} + (\nabla \cdot \boldsymbol{v}) \quad\quad = 0. \tag{A4}$$

Thus,

$$\frac{D(s)}{Dt} \equiv -(\nabla \cdot \boldsymbol{v}), \tag{A5}$$

where $s = \ln(\rho/\rho_0)$. Thus, we have a connection between the time evolution of the density (the Ds/Dt term) and the gas dynamics (as represented by the velocity vector, $\boldsymbol{v}$).

However, we can also derive the Lagrangian continuity equation from the Eulerian formulation. From the standard Eulerian continuity equation, we find

$$\frac{\partial \rho}{\partial t} + \nabla \cdot (\rho \boldsymbol{v}) = 0;$$
$$\Longleftrightarrow \quad \frac{\partial \rho}{\partial t} + (\boldsymbol{v} \cdot \nabla)\rho = -\rho \nabla \cdot \boldsymbol{v};$$
$$\Longleftrightarrow \quad \frac{1}{\rho} \frac{D\rho}{Dt} = -\nabla \cdot \boldsymbol{v};$$
$$\Longleftrightarrow \quad \frac{Ds}{Dt} = -\nabla \cdot \boldsymbol{v}; \tag{A6}$$

where the Lagrangian (comoving) derivative $D/Dt = \partial/\partial t + (\boldsymbol{v} \cdot \nabla)$, and $s = \ln(\rho/\rho_0)$ were used in the last two steps.

Appendix B
Analysis of Run GTMJ

In Sections 3 through 5, we focused on run GTMJR and did not show the results for run GTMJ since the differences between these runs for the purposes of our analysis are minimal. We found that including both lines in our figures significantly cluttered our plots without substantially enhancing the understanding of our results. However, for completeness, we use this appendix to present Figures 6, 7, and 8 with run GTMJ also shown.

Figure 10 reproduces Figure 6 with the addition of run GTMJ. Very little difference can be found between runs GTMJ and GTMJR, although there seems to be slightly more time variation in run GTMJR for the net rate at the lowest densities.

Figure 11 reproduces Figure 7 with the addition of run GTMJ. Again, there is very little difference between runs GTMJ and GTMJR. In fact, the mean SFRs are almost identical. The inclusion of radiative heating in run GTMJR appears to slightly lower the median value of the compressing gas mass flux relative to run GTMJ near $s \sim 6.5$; however, the difference is small and well within the 1σ time variation of both runs.

Figure 12 reproduces Figure 8 with the addition of run GTMJ. Again, there is very little difference between runs GTMJ and GTMJR. Indeed, the value of s_* is very similar for the two runs, as can be seen in Table 2.
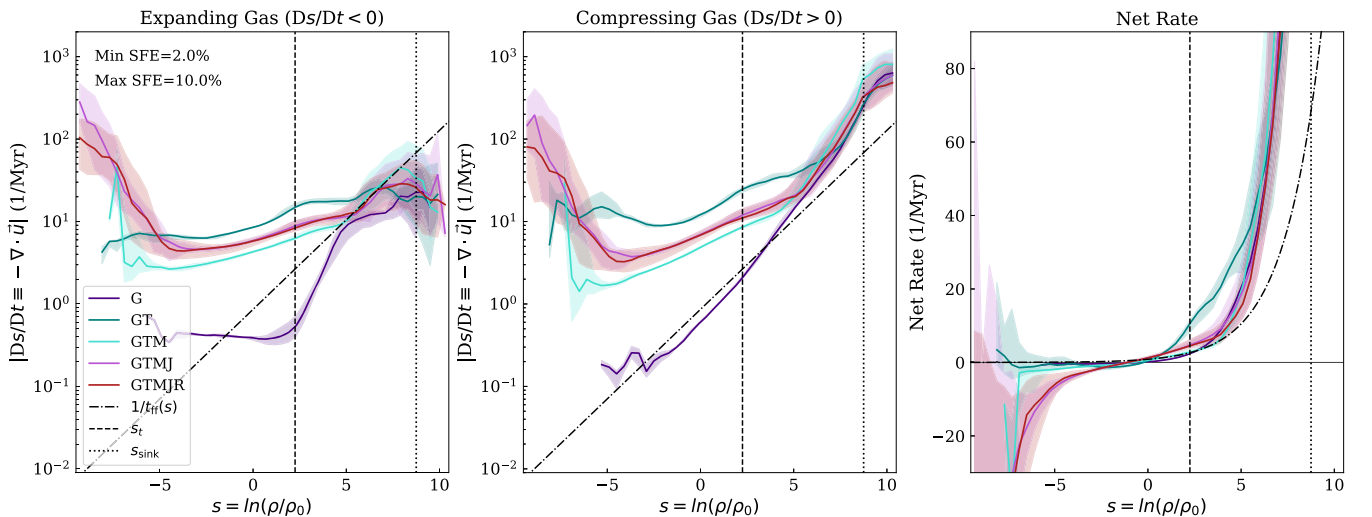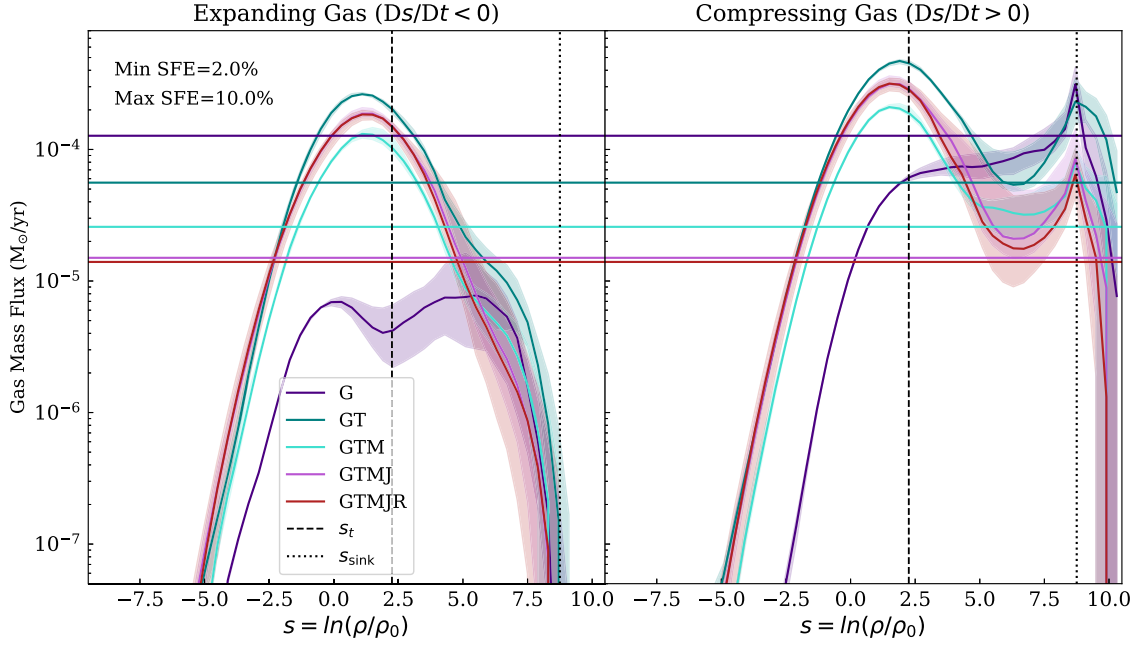

Figure 10. Figure 6 with run GTMJ.

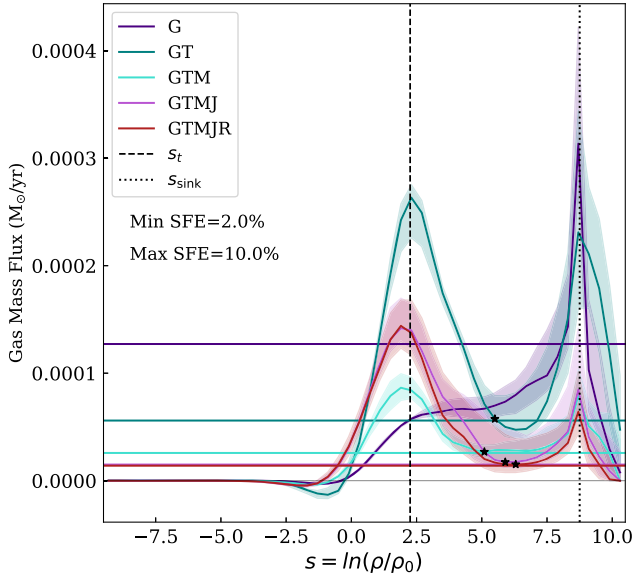**Figure 11.** Figure 7 with run GTMJ.

Figure 12. Figure 8 with run GTMJ.

Appendix C
Analysis of Run GTMJRD

As discussed in Section 2, we run an additional, sixth simulation, run GTMJRD, for which turbulence driving is turned off after the initial two turnover times. Although our results are not substantially changed in this case, we present here versions of some of our key plots with this run included for comparison. The analysis for these plots is the same as that described in the main body of the paper. To speed up calculations, Figures 14 through 16 are constructed using only every tenth snapshot, resulting in a slightly coarser time resolution than the figures in the main body of the paper.

In Figure 13, we consider the SFR and the integrated SFR for run GTMJRD, as in Figure 2 in the main body of the paper.
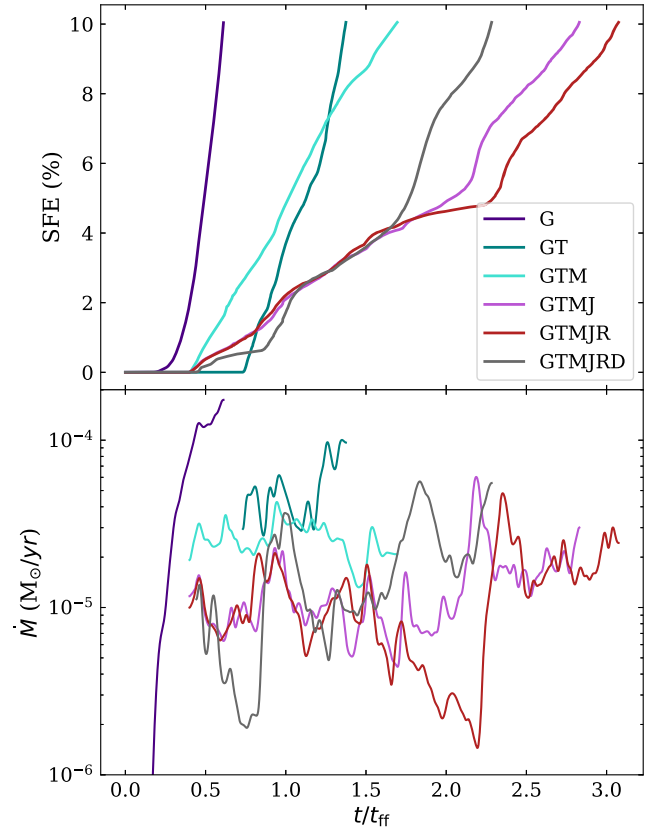

Figure 13. Figure 2 with runs GTMJ and GTMJRD, which includes decaying turbulence instead of continuous turbulence driving.

We find that the evolution of the SFE for the run with decaying turbulence is extremely similar to that of run GTMJR at early times. However, at later times, the turbulence decays away, and the SFR increases in run GTMJRD relative to run GTMJR and the SFE increases more rapidly. This behavior is exactly as we expect based on previous work, such as Federrath (2015) and
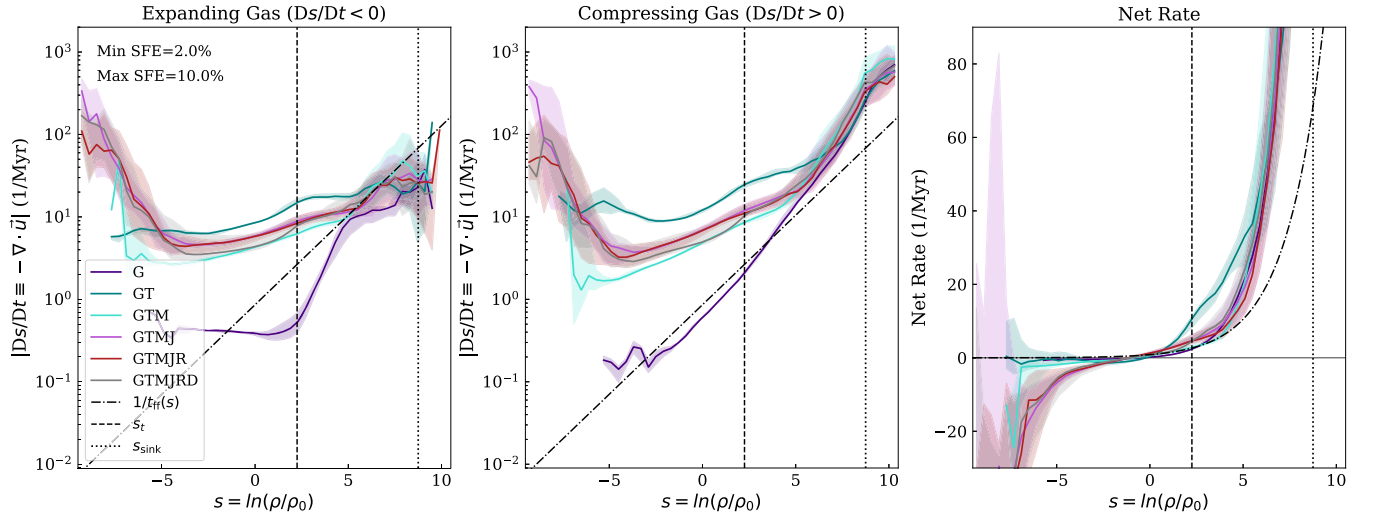
Figure 14. Figure 6 with runs GTMJ and GTMJRD, which includes decaying turbulence instead of continuous turbulence driving.
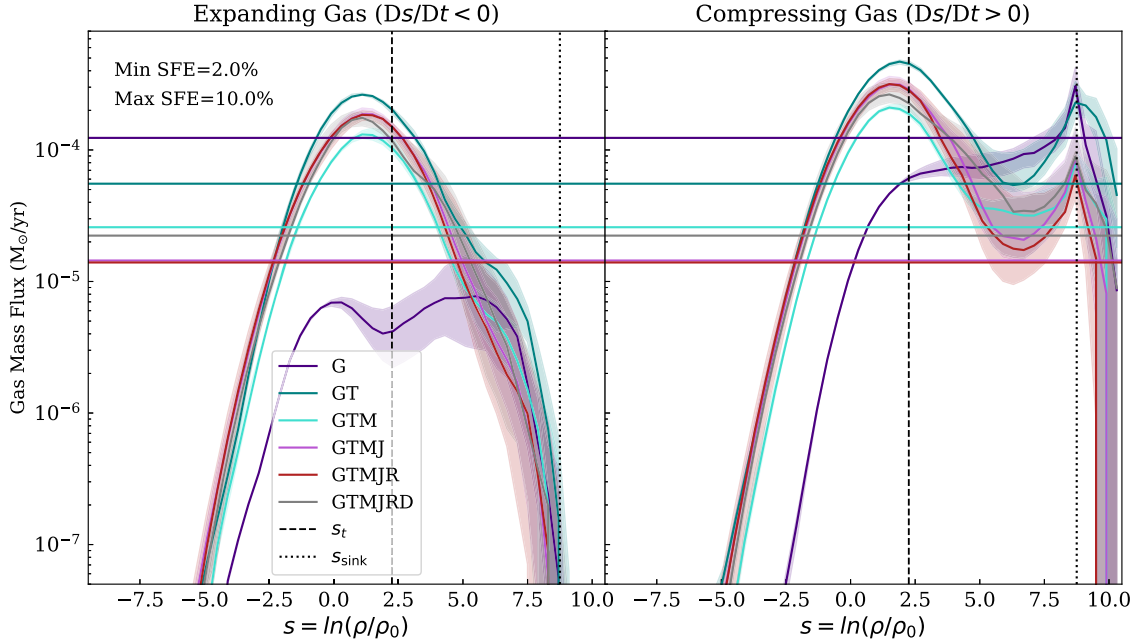

Figure 15. Figure 7 with runs GTMJ and GTMJRD, which includes decaying turbulence instead of continuous turbulence driving.

Appel et al. (2022), which shows that driven turbulence serves to decrease the SFR.

In Figure 14 (a modified version of Figure 6), we also see that the run with decaying turbulence exhibits very similar expansion, compression, and net rates to the feedback runs with driven turbulence. The key features of the rates discussed with respect to Figure 6 are present in the run with decaying turbulence. That is, the expansion and compression rates for run GTMJRD match those of the gravity-only run at high densities. In addition, run GTMJRD has increased expansion and compression rates at low densities due to the influence of feedback.

We also plot the median gas mass flux values in Figure 15 (as in Figure 7), along with the mean SFR. We see that, while the mean SFR is higher for the run with decaying turbulence than in the runs with driven turbulence, the overall behavior of the decaying turbulence run is similar to that of runs GTMJ and GTMJR.

Indeed, in Figure 16 (which reproduces Figure 8 but with run GTMJRD), we see that the net gas mass flux for run GTMJRD follows a similar overall behavior to the runs with driven turbulence. The gas mass flux for the decaying turbulence run also peaks around s_t before dropping off, briefly leveling out, and peaking again at $s_{\rm sink}$. We note that the lowest point of the net gas mass flux does not quite reach the mean SFR for the new decaying turbulence run, as it does for runs GTMJ and GTMJR. However, this is likely due to stochastic variations of the mass flux and the SFR and does not substantially change our results. For example, the lowest point of run GT is well below the mean SFR. In addition, the 1σ variation in time (the shaded region) does overlap with the mean SFR. We define the value of s_* to be the point of closest approach between the mean SFR and the net gas mass flux and find that the value of s_* for this run corresponds to the same bin as that for run GTMJR.
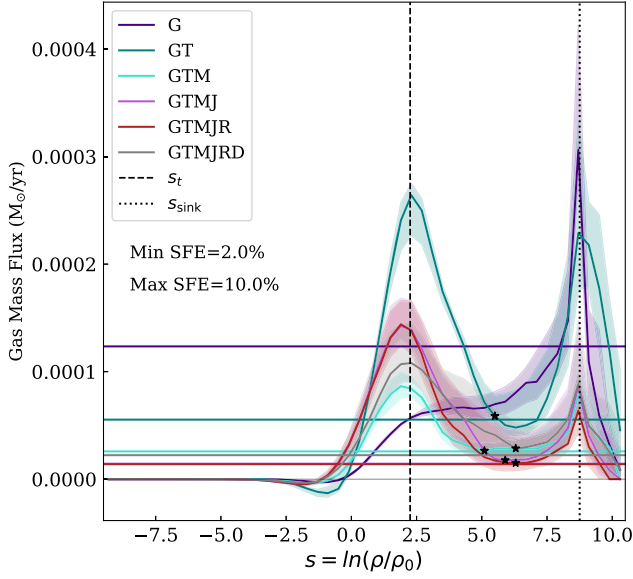
Figure 16. Figure 8 with runs GTMJ and GTMJRD, which includes decaying turbulence instead of continuous turbulence driving.

Overall, we find that our results stay qualitatively similar in a run with decaying turbulence. Run GTMJRD has an overall higher SFR than the corresponding run with driven turbulence, especially at late times as the turbulence decays. However, this does not change the behavior of the compression and expansion rates or the gas mass flux.

Appendix D
Check Time Variation of the Density PDF

Similar to the upper panels of Figure 4, Figure 17 shows a comparison between the overall PDF and the expanding or compressing PDF for all four physics cases (we do not include run GTMJ here). We show three different points in time for each simulation, corresponding to just before the formation of the first sink particle (SFE = 0%), the approximate midpoint of each simulation (SFE = 5%), and the end of each simulation (SFE = 10%). For all four physics cases and all three points in time, the same trend is apparent. At high densities, the overall density PDF is well matched by the compressing gas PDF but is much higher than the expanding gas PDF. However, at low densities, the overall PDF is well matched by the expanding gas
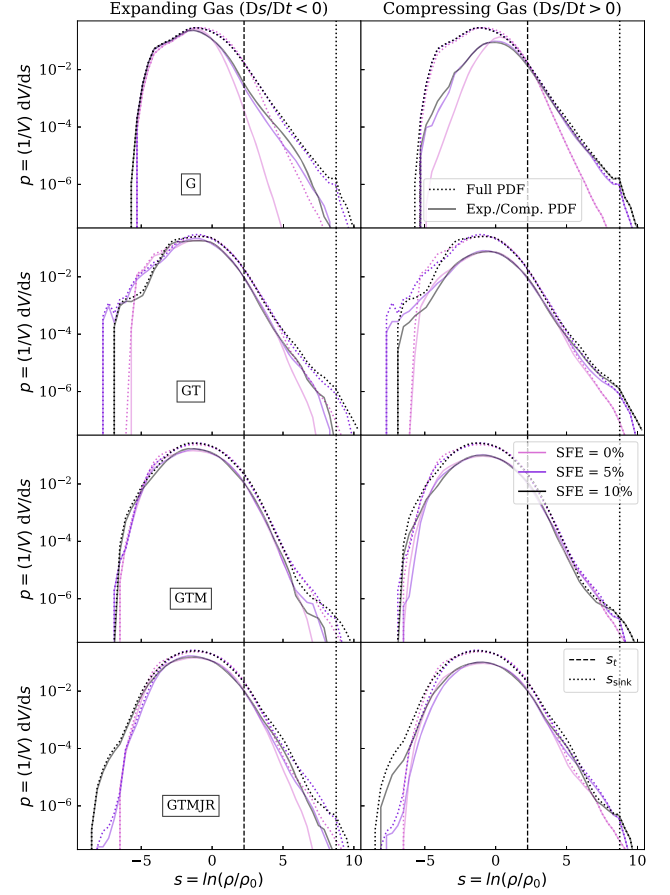

Figure 17. Each panel shows the volume-weighted density PDF for all of the gas in the simulation region (dotted line) and the volume-weighted density PDF for only the expanding gas ($Ds/Dt < 0$; left column) or only the compressing gas ($Ds/Dt > 0$; right column) within the simulation region. Each row shows a different simulation, and the color corresponds to three different points in time (SFE = 0%, 5%, 10%). As in Figure 4, the transition density (s_t) from Appel et al. (2022) is overplotted. The sink formation density threshold (s_{sink}) for the simulation is also shown.

PDF but diverges from the compressing gas PDF. This confirms that most of the expanding gas is at low densities while the compressing gas is predominantly at high densities. The transition between these regimes is continuous and fairly gradual.

ORCID iDs

Sabrina M. Appel ⓘ https://orcid.org/0000-0002-6593-3800
Blakesley Burkhart ⓘ https://orcid.org/0000-0001-5817-5944
Vadim A. Semenov ⓘ https://orcid.org/0000-0002-6648-7136
Christoph Federrath ⓘ https://orcid.org/0000-0002-0706-2306
Anna L. Rosen ⓘ https://orcid.org/0000-0003-4423-0660
Jonathan C. Tan ⓘ https://orcid.org/0000-0002-3389-9142

References

Alves, J., Lombardi, M., & Lada, C. J. 2017, A&A, 606, L2
Appel, S. M., Burkhart, B., Semenov, V. A., Federrath, C., & Rosen, A. L. 2022, ApJ, 927, 75
Astropy Collaboration, Robitaille, T. P., Tollerud, E. J., et al. 2013, A&A, 558, A33
Ballesteros-Paredes, J., Hartmann, L. W., Vázquez-Semadeni, E., Heitsch, F., & Zamora-Avilés, M. A. 2011, MNRAS, 411, 65
Ballesteros-Paredes, J., & Mac Low, M.-M. 2002, ApJ, 570, 734
Berger, M. J., & Colella, P. 1989, JChPh, 82, 64
Braun, H., & Schmidt, W. 2015, MNRAS, 454, 1545
Burkhart, B. 2018, ApJ, 863, 118
Burkhart, B., & Lazarian, A. 2012, ApJL, 755, L19
Burkhart, B., & Mocz, P. 2019, ApJ, 879, 129
Burkhart, B., Stalpes, K., & Collins, D. C. 2017, ApJL, 834, L1
Chen, H. H.-H., Pineda, J. E., Goodman, A. A., et al. 2019, ApJ, 877, 93
Collins, D. C., Kritsuk, A. G., Padoan, P., et al. 2012, ApJ, 750, 13
Cournoyer-Cloutier, C., Sills, A., Harris, W. E., et al. 2023, MNRAS, 521, 1338
Crutcher, R. M., Wandelt, B., Heiles, C., Falgarone, E., & Troland, T. H. 2010, ApJ, 725, 466
Dubey, A., Fisher, R., Graziani, C., et al. 2008, in ASP Conf. Ser. 385, Numerical Modeling of Space Plasma Flows, ed. N. V. Pogorelov, E. Audit, & G. P. Zank (San Francisco, CA: ASP), 145
Falgarone, E., Puget, J. L., & Perault, M. 1992, A&A, 257, 715
Falgarone, E., Troland, T. H., Crutcher, R. M., & Paubert, G. 2008, A&A, 487, 247
Federrath, C. 2015, MNRAS, 450, 4035
Federrath, C. 2016a, JPlPh, 82, 535820601
Federrath, C. 2016b, MNRAS, 457, 375
Federrath, C., & Klessen, R. S. 2012, ApJ, 761, 156
Federrath, C., & Klessen, R. S. 2013, ApJ, 763, 51
Federrath, C., Klessen, R. S., Iapichino, L., & Beattie, J. R. 2021, NatAs, 5, 365
Federrath, C., Klessen, R. S., & Schmidt, W. 2008, ApJ, 688, L79
Federrath, C., Krumholz, M., & Hopkins, P. F. 2017a, JPhCS, 837, 012007
Federrath, C., Roman-Duval, J., Klessen, R. S., Schmidt, W., & Mac Low, M.-M. 2010, A&A, 512, A81
Federrath, C., Roman-Duval, J., Klessen, R. S., Schmidt, W., & Mac Low, M. M. 2022, TG: Turbulence Generator, Astrophysics Source Code Library, ascl:2204.001
Federrath, C., Salim, D. M., Medling, A. M., et al. 2017b, MNRAS, 468, 3965
Federrath, C., Schrön, M., Banerjee, R., & Klessen, R. S. 2014, ApJ, 790, 128
Federrath, C., Sur, S., Schleicher, D. R. G., Banerjee, R., & Klessen, R. S. 2011, ApJ, 731, 62
Fryxell, B., Olson, K., Ricker, P., et al. 2000, ApJS, 131, 273
Gensior, J., Kruijssen, J. M. D., & Keller, B. W. 2020, MNRAS, 495, 199
Guszejnov, D., Grudić, M. Y., Hopkins, P. F., Offner, S. S. R., & Faucher-Giguère, C.-A. 2020, MNRAS, 496, 5072
Hennebelle, P., & Chabrier, G. 2008, ApJ, 684, 395
Hennebelle, P., & Chabrier, G. 2009, ApJ, 702, 1428
Hennebelle, P., & Chabrier, G. 2011, ApJL, 743, L29
Hopkins, P. F., Quataert, E., & Murray, N. 2012, MNRAS, 421, 3488
Hull, C. L. H., Mocz, P., Burkhart, B., et al. 2017, ApJL, 842, L9

Hunter, J. D. 2007, CSE, 9, 90
Imara, N., & Burkhart, B. 2016, ApJ, 829, 102
Jaupart, E., & Chabrier, G. 2020, ApJL, 903, L2
Kainulainen, J., Beuther, H., Henning, T., & Plume, R. 2009, A&A, 508, L35
Kennicutt, R. C., & Evans, N. J. 2012, ARA&A, 50, 531
Khullar, S., Federrath, C., Krumholz, M. R., & Matzner, C. D. 2021, MNRAS, 507, 4335
Khullar, S., Krumholz, M. R., Federrath, C., & Cunningham, A. J. 2019, MNRAS, 488, 1407
Kitsionas, S., Federrath, C., Klessen, R. S., et al. 2009, A&A, 508, 541
Klessen, R. S. 2000, ApJ, 535, 869
Kretschmer, M., & Teyssier, R. 2020, MNRAS, 492, 1385
Kritsuk, A. G., Nordlund, Å., Collins, D., et al. 2011a, ApJ, 737, 13
Kritsuk, A. G., Norman, M. L., & Wagner, R. 2011b, ApJL, 727, L20
Krumholz, M. R., Burkhart, B., Forbes, J. C., & Crocker, R. M. 2018, MNRAS, 477, 2716
Krumholz, M. R., & McKee, C. F. 2005, ApJ, 630, 250
Lane, H. B., Grudić, M. Y., Guszejnov, D., et al. 2022, MNRAS, 510, 4767
Lewis, S. C., McMillan, S. L. W., Low, M.-M. M., et al. 2023, ApJ, 944, 211
Ma, Y., Wang, H., Zhang, M., et al. 2022, ApJS, 262, 16
Masunaga, H., & Inutsuka, S.-i 2000, ApJ, 531, 350
Mathew, S. S., & Federrath, C. 2020, MNRAS, 496, 5201
Mathew, S. S., & Federrath, C. 2021, MNRAS, 507, 2448
McKee, C. F., & Ostriker, E. C. 2007, ARA&A, 45, 565
Myers, A. T., Klein, R. I., Krumholz, M. R., & McKee, C. F. 2014, MNRAS, 439, 3420
Nam, D. G., Federrath, C., & Krumholz, M. R. 2021, MNRAS, 503, 1138
Offner, S. S. R., Klein, R. I., McKee, C. F., & Krumholz, M. R. 2009, ApJ, 703, 131
Padoan, P., & Nordlund, Å. 2011a, ApJL, 741, L22
Padoan, P., & Nordlund, Å. 2011b, ApJ, 730, 40
Padoan, P., Federrath, C., Chabrier, G., et al. 2014, in Protostars and Planets VI, ed. H. Beuther et al. (Tuscon, AZ: Univ. Arizona Press), 77
Padoan, P., Haugbølle, T., & Nordlund, Å. 2012, ApJL, 759, L27
Padoan, P., Nordlund, A., & Jones, B. J. T. 1997, MNRAS, 288, 145
Passot, T., & Vázquez-Semadeni, E. 2003, A&A, 398, 845
Passot, T., Vazquez-Semadeni, E., & Pouquet, A. 1995, ApJ, 455, 536
Pedregosa, F., Varoquaux, G., Gramfort, A., et al. 2011, JMLR, 12, 2825
Price, D. J., & Federrath, C. 2010, MNRAS, 406, 1659
Ricker, P. M. 2008, ApJS, 176, 293
Rosdahl, J., Katz, H., Blaizot, J., et al. 2018, MNRAS, 479, 994
Rosen, A. L., Krumholz, M. R., McKee, C. F., & Klein, R. I. 2016, MNRAS, 463, 2553
Schneider, N., Bontemps, S., Girichidis, P., et al. 2015, MNRAS Lett., 453, L41
Seifried, D., Walch, S., Girichidis, P., et al. 2017, MNRAS, 472, 4797
Semenov, V. A., Kravtsov, A. V., & Gnedin, N. Y. 2016, ApJ, 826, 200
Semenov, V. A., Kravtsov, A. V., & Gnedin, N. Y. 2017, ApJ, 845, 133
Semenov, V. A., Kravtsov, A. V., & Gnedin, N. Y. 2018, ApJ, 861, 4
Semenov, V. A., Kravtsov, A. V., & Gnedin, N. Y. 2021, ApJ, 918, 13
Stutz, A. M., & Kainulainen, J. 2015, A&A, 577, L6
Trebitsch, M., Blaizot, J., Rosdahl, J., Devriendt, J., & Slyz, A. 2017, MNRAS, 470, 224
Truelove, J. K., Klein, R. I., McKee, C. F., et al. 1997, ApJL, 489, L179
Turk, M. J., Smith, B. D., Oishi, J. S., et al. 2011, ApJS, 192, 9
Vazquez-Semadeni, E. 1994, ApJ, 423, 681
Vazquez-Semadeni, E., Ballesteros-Paredes, J., & Rodriguez, L. F. 1997, ApJ, 474, 292
Vazquez-Semadeni, E., & Garcia, N. 2001, ApJ, 557, 727
Virtanen, P., Gommers, R., Oliphant, T. E., et al. 2020, NatMe, 17, 261
Waagan, K., Federrath, C., & Klingenberg, C. 2011, JCoPh, 230, 3331
Wang, P., Li, Z., Abel, T., & Nakamura, F. 2010, ApJ, 709, 27
Wu, B., Tan, J. C., Christie, D., et al. 2017, ApJ, 841, 88
Zamora-Avilés, M., Vázquez-Semadeni, E., Körtgen, B., Banerjee, R., & Hartmann, L. 2018, MNRAS, 474, 4824